HONO chemistry at a suburban site during the EXPLORE-YRD campaign in 2018: ~~HONO~~ formation mechanisms and impacts on O₃ production

Can Ye[1], Keding Lu[1], Xuefei Ma[1], Wanyi Qiu[1], Shule Li[1], Xinping Yang[2], Chaoyang Xue[3], Tianyu Zhai[1], Yuhan Liu[1], Xuan Li[1], Yang Li[1], Haichao Wang[1], Zhaofeng Tan[1], Xiaorui Chen[1], Huabin Dong[1], Limin Zeng[1], Min Hu[1], Yuanhang Zhang[1]

[1] State Key Joint Laboratory of Environment Simulation and Pollution Control, College of Environmental Sciences and Engineering, Peking University, Beijing, 100871, China
[2] State Environmental Protection Key Laboratory of Vehicle Emission Control and Simulation, Chinese Research Academy of Environmental Sciences, Beijing, 100012, China
[3] Max Planck Institute for Chemistry, Mainz 55128, Germany

Correspondence to: Keding Lu (k.lu@pku.edu.cn), Yuanhang Zhang(yhzhang@pku.edu.cn)

Abstract. HONO is an important precursor for OH radicals that impact secondary pollutants production. However, there are still large uncertainties about different HONO sources, which hinder accurate predictions of HONO concentration and hence atmospheric oxidation capacity. Here HONO was measured during the EXPLORE-YRD campaign, along with other important parameters, enabling us to comprehensively investigate HONO variation characteristics and evaluate the relative importance of different HONO sources by using a box model. HONO showed significant variations, ranging from several tens of ppt to 4.4 ppb. The average diurnal pattern of HONO/NO$_x$ showed a maximum of 0.17 around noon and resembled that of j(O^{1}D), indicating the existence of photo-induced sources. Modeling simulations with only the default HONO source (OH+NO) largely underestimated HONO concentrations, with the modeled averaged noontime HONO concentration an order of magnitude lower than the observed concentration. The calculated unknown source strength (P$_{unknown}$) of HONO showed a nearly symmetrical diurnal profile with a maximum of 2.5 ppb h^{-1} around noon. The correlation analysis and sensitivity tests showed that photo-induced NO$_2$ conversion on the ground was able to explain P$_{unknown}$. Additional HONO sources incorporated into the box model improved the model's performance in simulating HONO concentrations. The revised box model well reproduced nighttime HONO concentration but still underestimated daytime HONO concentration. Further sensitivity tests indicated the underestimation of daytime HONO was not due to uncertainties of photo-induced NO$_2$ uptake coefficients on the ground or aerosol surfaces or enhancement factor of nitrate photolysis but was more likely due to other sources that were not considered in the model. Among the incorporated heterogeneous HONO sources, vehicle emission, and the gas-phase source, photo-induced NO$_2$ conversion on the ground dominated the modeled HONO production during the daytime, accounting for ~~73~~71% of the total, followed by NO+OH ~~(10%)~~, NO$_2$ hydrolysis on the

ground surface ~~(9%)~~, vehicle emission, photo-induced NO_2 conversion on the aerosol surface ~~(3%)~~, nitrate photolysis ~~(3%)~~, and NO_2 hydrolysis on the aerosol surface (2%). NO_2 hydrolysis on the ground surface was the major source of nighttime HONO, contributing to 65% of total HONO production. HONO photolysis contributed to 43% of RO_x production during the daytime, followed by O_3 photolysis (17%), HCHO photolysis (14%), ozonolysis of alkenes (12%), and carbonyl photolysis (10%). The net ozone production rate (~~12.6~~6.7 ppb h^{-1}) ~~with~~ without observed HONO as a model constraint ~~decreased~~ increased by ~~45~~88% compared to that (~~6.7~~12.6 ppb h^{-1}) ~~without~~ with HONO as a model constraint, indicating HONO evidently enhanced O_3~~HONO~~ production and hence aggravated O_3 pollution in summer seasons. Our study emphasized the importance of NO_2 heterogeneous conversion on the ground surface in HONO production and accurate parameterization of HONO sources in predicting secondary pollutants production.

1 Introduction

OH radicals are the primary oxidant in the atmosphere, accelerating the degradation of gas-phase pollutants and regulating the lifetime of trace gases. OH oxidation will lead to secondary pollutants formation like secondary organic aerosol (SOA) and O_3, which both have adverse impacts on air quality. HONO is one of the most important precursors of OH radicals by photolysis (R1), especially in polluted areas, contributing to up to 92% of primary OH production (Alicke et al., 2003; Kleffmann et al., 2005; Elshorbany et al., 2009; Hou et al., 2016; Xue et al., 2020; Tan et al., 2017). Previous studies reported that HONO was ~~not only an~~ a vital OH precursor not only in the early morning but also throughout the day (Neftel et al., 1996; Ren et al., 2003; Ren et al., 2006; Michoud et al., 2012). Therefore, HONO is closely linked to atmospheric oxidation capacity, and accurate representation of HONO sources in models is important for air quality predictions and control strategy development.

$$HONO \xrightarrow{h\nu} OH+NO \tag{R1}$$

$$OH+NO \xrightarrow{M} HONO \tag{R2}$$

However, HONO sources are still controversially discussed due to the complexity of their formation mechanisms. Till now, several HONO sources, including gas-phase reactions, direct emissions, heterogeneous reactions on ~~varied~~ various surfaces, and acid displacement reactions, have been proposed ~~to explain HONO~~. The gas-phase HONO source mainly comes from the reaction between OH and NO (R2). This source is too small to explain high HONO levels frequently observed at different sites in the world (Lee et al., 2016; Michoud et al., 2014; Liu et al., 2019b; Kleffmann et al., 2003), indicating there still exist other sources. Large HONO unknown sources were reported at different sites, for instance, 3 ppb h^{-1} in Tai'an (Xue et al., 2022), 2.58 ppb h^{-1} in Beijing (Spataro et al., 2013), 0.7 ppb h^{-1} in Paris (Michoud et al., 2014), 1.77 ppb h^{-1} in Santiago (Elshorbany et al., 2009). The unknown source strength was one magnitude higher than the HONO production rate by the OH+NO reaction. Other gas-phase sources, like the reaction

2

60 between excited NO_2 and water molecules (Li et al., 2008) and the photolysis of nitro-phenols (Bejan et al., 2006), have also been proposed. However, the two gas-phase sources were verified to be of minor importance to HONO production under atmospherically relevant conditions (Yang et al., 2021a; Sorgel et al., 2011). Direct emissions include emissions from combustion sources and fertilized soil by biological processes. HONO could be directly released from vehicle exhausts and is often characterized by the $HONO/NO_x$ ratio, which is typically less than 2% NO_x

65 emissions (Kurtenbach et al., 2001; Xu et al., 2015; Kramer et al., 2020). Hence, HONO emissions by vehicles were considered to play a minor role in HONO formation, especially in rural and remote areas. Biomass burning and wildfire also contributed to HONO emissions on a global scale (Nie et al., 2015; Cui et al., 2021). HONO emitted by wildfires was estimated to account for two-thirds of OH production in fresh wildfire plumes, which accelerated the age of plumes and O_3 production (Theys et al., 2020). In addition, microbe-produced nitrite from fertilized soil can

70 produce HONO (Su et al., 2011; Oswald et al., 2013; Weber et al., 2015; Scharko et al., 2015; Wang et al., 2021). Recent field studies revealed HONO and concurrent O_3 and H_2O_2 enhancements after fertilization events in the North China Plain, implying the large impact of soil-emitted HONO on regional atmospheric oxidation capacity (Xue et al., 2021).

$$NO_2 + H_2O \xrightarrow{surfaces} HONO + HNO_3 \qquad\qquad R3$$

$$NO_2 + A^{red} \rightarrow HONO + A^{"} \qquad\qquad R4$$

$$HNO_{3(ads)} \xrightarrow{hv} [HNO_3]^*_{ads} \qquad\qquad R5$$

$$[HNO_3]^*_{ads} \rightarrow HONO_{ads} + O_{ads} \qquad\qquad R6$$

Heterogeneous processes are believed to be important for HONO production. Heterogeneous NO_2 conversion on

75 humid surfaces (R3) has long been identified as an important source of nighttime HONO, with two NO_2 molecules converting to one HONO molecule (Finlayson-Pitts et al., 2003; Stutz et al., 2004). However, R3 could not explain HONO levels during the daytime. Field measurements revealed HONO unknown source was ~~typically~~ positively correlated with $j(NO_2)$, indicating a photo-induced process (Vogel et al., 2003; Lee et al., 2016). Photo-induced NO_2 conversion on humic acid was proposed to explain daytime HONO (R4) (Stemmler et al., 2006; Stemmler et al., 2007).

80 This source was found to be important to sustain high daytime HONO levels (Wong et al., 2013; Zhang et al., 2016; Xue et al., 2022). In addition, ~~heterogeneous~~ adsorbed nitrate/HNO_3 photolysis on ~~varied~~ various surfaces was found to be enhanced compared to gas-phase HNO_3 and also contributed to HONO formation (Zhou et al., 2011; Ye et al., 2016; Ye et al., 2017; Bao et al., 2018; Baergen and Donaldson, 2013). However, the importance of heterogeneous nitrate/HNO_3 photolysis on HONO production (R5-R6) is highly uncertain, with the enhancement factor (EF) for

85 nitrate photolysis relative to gas-phase nitric acid spanning three orders of magnitude from 1 to 1000 (Ye et al., 2017; Bao et al., 2018; Laufs and Kleffmann, 2016; Romer et al., 2018; Shi et al., 2021). HONO deposition during the

nighttime and subsequent desorption from the soil by strong acid displacement during the daytime was proposed to be a HONO source (Vandenboer et al., 2015). Although ~~varied~~ various sources have been proposed, there are still large uncertainties about many mechanisms and the relative importance of each mechanism in different environments.

90 O_3 pollution is serious in China in the summer and becomes a major air quality issue. The observed ozone-increasing rates from 2013-2017 were 3.11 ppb year^{-1}, 2.29 ppb year^{-1}, 0.56 ppb year^{-1}, and 1.63 ppb year^{-1} in Beijing–Tianjin–Hebei (BTH), Yangtze River Delta (YRD), Pearl River Delta (PRD), and Sichuan Basin (SCB), respectively, the four megacity clusters in China (Li et al., 2019a). O_3 is produced by complex photochemical chain reactions between volatile organic compounds (VOCs) and NO_x in the presence of sunlight. Now the control strategy for O_3 pollution

95 mainly focuses on the reduction of VOC and NO_x, which mainly depend on the O_3 formation regimes. HONO photolysis is one of the major sources of primary RO_x radicals, which initiate the photochemical reactions leading to O_3 formation. More and more field studies and modeling studies found that high HONO levels in China aggravated O_3 pollution. For instance, the incorporation of proposed HONO sources improved the predictions of O_3 by the WRF-Chem model and increased O_3 concentrations by 6-12% compared with cases without HONO sources (Zhang et al.,

100 2016). Fu et al. (~~Fu et al.,~~ 2019) found that newly-added HONO sources increased nitrate concentrations by 17 µg m^{-3} and O_3 by 24 ppb during a winter pollution episode in the PRD of China. Furthermore, missing representations of HONO sources in box models or chemical transport models would affect the judgment of O_3 formation regimes and lead to ineffective O_3 mitigation strategies (Li et al., ~~2018b~~2018c; Liu et al., 2023b). Therefore, an accurate understanding of HONO formation mechanisms is important for the refinement of the O_3 pollution control policy.

105 YRD is one of the most populated and polluted areas in the world. Recently, this area has witnessed an evident increase in O_3 levels, with O_3 pollution days ~~nearly~~ more than doubling (28 days to 76 days) from 2014 to 2017 (Liu et al., 2020). Large numbers of studies were carried out that mainly focused on the study of O_3 pollution characteristics and determination of O_3 sensitivity to VOCs and NO_x (Ding et al., 2013; Xing et al., 2017; Wang et al., 2019), while research on HONO formation mechanisms and their effects on RO_x (OH, HO_2, RO_2 radicals) budget and O_3

110 production was still limited. The EXPLORE-YRD campaign (EXPeriment on the eLucidation of the atmospheric Oxidation capacity and aerosol foRmation, and their Effects in the Yangtze River Delta) was carried out with the aim of exploring the atmospheric oxidation capacity in the area and developing an effective co-control strategy for both O_3 and particulate matter. As mentioned above, HONO chemistry is closely linked to atmospheric oxidation capacity and, therefore, should be comprehensively studied. In this study, HONO was measured along with other gas-phase

115 (including OH, HO_2, VOCs, NO_x, etc.), aerosol-phase, and meteorological parameters during the EXPLORE-YRD campaign in China, allowing us a detailed evaluation of HONO chemistry by employing an observation-based box model. We first investigate the HONO variation characteristics and the unknown source strength. Then correlation analysis and sensitivity tests were performed to investigate the relative importance of different HONO sources

4

preliminarily. Then we incorporate proposed HONO sources into the box model to investigate if these sources could explain observed HONO concentration. The comparison of modeled and measured HONO provides unique information for understanding different HONO formation mechanisms and exploring their respective contributions to HONO production. Based on modeling results, the contribution of HONO photolysis to primary RO_x production was calculated. In addition, the O_3 formation rates calculated with and without HONO sources were also compared to investigate the effects of HONO on O_3 production.

2 Experimental

2.1 Site description

EXPLORE-YRD campaign was performed from May 14 to June 20, 2018 at a suburban site (32.56°N, 119.99°E) in the YRD region, one of the most polluted areas in China. The measurement site is located in the park of the meteorological radar station in Taizhou City, which is situated 200 km northwest of Shanghai City (Figure 1S1). This site was surrounded by farmlands and fishponds and far away from industrial areas, occasionally influenced by biomass-burning events. Winds from the east and southeast prevailed during the measurement periods, indicating this site is influenced by anthropogenic pollution from the YRD region. All the instruments were placed in five containers, and the sampling inlet was about 5 m above the ground.

2.2 HONO measurement

HONO was measured by a commercial HONO monitor (LOPAP, QUMA), which was based on a wet chemical technique. A detailed description of the instrument has been introduced in previous studies (Heland et al., 2001; Xue et al., 2020). Briefly, HONO was sampled by stripping solution (sulfanilamid + HCl) in a stripping coil. Then the sampled solution will react with n-(1-naphthyl)-ethylenediamine-dihydrochloride solution, yielding azo dye, which will be detected by an optical absorption spectrometer at 550 nm. In order to minimize the effect of interfering species, two stripping coils in series were employed. In the first coil, nearly all HONO and a small fraction of interfering species was sampled. In the second coil, assuming the same amount of interfering species was sampled, the difference in signals between the two coils represents the true HONO concentration in the atmosphere. Zero calibration was performed every day. The detection limit and uncertainty of the instrument were 5 ppt and 10%, respectively.

2.3 Other measurements

A comprehensive set of gas-phase and aerosol-phase parameters has been measured in the campaign, and detailed information on parameters and instruments is listed in Table S1 in the supporting information. Here we will make a

5

brief introduction. O_3, CO, SO_2, and $PM_{2.5}$ were measured by Model 49i, Model 48i, Model 43i and Model 1400A from Thermo Inc, respectively. NO_x was measured by a trace-level analyzer (Model 42i), which was equipped with a home-built photolytic converter for true NO_2 measurement to avoid interference from other NO_y species like peroxyacetyl nitrate (PAN), HONO, and organic nitrate. As NO_2 was an important precursor of HONO, true NO_2 measured was used ~~throughout the paper~~in this study to better understand HONO formation mechanisms. VOCs were measured by an online gas chromatograph equipped with a flame ionization detector and mass spectrometry. HCHO was measured by the Hantzsch fluorescence technique. OH and HO_2 radicals were measured by PKU-LIF, and detailed information about PKU-LIF equipment can be found in our previous studies (Lu et al., 2013; Tan et al., 2017; Ma et al., 2022). Photolysis frequencies were calculated using spectroradiometer-measured integrated actinic flux. RH, temperature, pressure, wind speed, and wind direction were simultaneously measured by a portable weather station (MAWS301, Vaisala, Finland). The aerosol surface area (S_a) was derived from data measured by a scanning mobility particle sizer instrument (SMPS, TSI 3936) and an aerosol particle sizer instrument (APS, TSI 3321). Aerosol-phase water-soluble ions were measured by a gas and aerosol collector equipped ion chromatography (GAC) instrument.

2.4 Observation-based box model

HONO concentration was simulated by a box model based on the RACM2-LIM1 mechanism. The model was constrained with measurements of NO, NO_2, O_3, CO, H_2O, C2-C12 VOCs, HCHO, OH radicals, temperature, and pressure with a time resolution of 5 min. Measured HONO was only constrained when trying to explore the contribution of HONO to primary RO_x budget and O_3 production rate. In other cases, HONO was not constrained in model simulations. In addition, $j(O^1D)$, $j(HONO)$, $j(H_2O_2)$, $j(NO_2)$ and $j(HCHO)$ were also constrained to the model. CH_4 and H_2 were assumed to be 1900 ppb and 550 ppb, respectively. In RACM2, based on the reactivities with OH, different VOCs were assigned to different lumped species rather than treated individually. A first-order dilution loss term with a lifetime of 8 hours was assigned to all species to represent deposition and advection loss. The modeled PAN and observed PAN matched well (Figure ~~S1~~S2), and the ratio of modeled to observed PAN concentration was 1.09 if this dilution term was incorporated. Detailed information on the box model can be found in our previous studies focusing on simulating OH and HO_2 radicals (Tan et al., 2017; Tan et al., 2018; Ma et al., 2019).

2.5 Ozone production rate calculation

The total ozone production rate ($F(O_3)$) was directly determined by the reactions between NO and peroxy radicals (Eq. 1). Due to a lack of measurements of different peroxy radical species, model-calculated peroxy radical concentrations were used in Eq. 1. O_3 was mainly consumed by photolysis and reactions with alkenes, OH, and HO_2. In addition, the reaction between OH and NO_2 forms HNO_3, which constitutes a portion of the O_3 loss. NO_3 radicals, formed by the

6

reaction between NO_2 and O_3, could subsequently form N_2O_5 or organic nitrate formation, contributing to O_3 loss. The loss rate of O_3 can be described in Eq. 2. Therefore, the net ozone production rate $P(O_3)$ can be obtained by calculating the difference between $F(O_3)$ and $D(O_3)$ (Eq. 3).

$$F(O_x)=k_{NO+HO_2}[NO][HO_2]+\sum_i k_{RO_{2i}+NO}[RO_2]_i[NO] \tag{1}$$

$$D(O_x)=k_{O^1D+H_2O}[O^1D][H_2O]+[O_3]\left(k_{O_3+Alkenes}[Alkenes]+k_{O_3+HO_2}[HO_2]+k_{O_3+OH}[OH]\right)+k_{OH+NO_2}[NO_2][OH]+$$
$$3\left(k_{O_3+NO_2}[NO_2][O_3]-k_{NO+NO_3}[NO_3][NO]-j_{NO_3}[NO_3]\right) \tag{2}$$

$$P(O_x)=F(O_x)-D(O_x) \tag{3}$$

3 Results and discussion

3.1 Overview of the measurements

Figure ~~2~~1. presents the time profiles of HONO and related chemical species as well as meteorological conditions from May 23 to June 18, 2018. The temperature ranged from 15 ℃ to 35 ℃, and the ~~relative humidity~~RH ranged from 30% to 100% during the measurement period. Rainfall events occurred on May 25, 26, and June 10, and corresponding concentrations of both primary and secondary pollutants were low as a result of low solar radiation intensity and the scouring effect of rain. The daily maximum values of $j(O^1D)$ frequently exceeded 2×10^{-5} s^{-1}, indicating strong solar radiation intensity during most days of the measurement period. The mean diurnal profiles of HONO and related parameters are shown in Figure ~~3~~2. ~~The maximum diurnal averaged HCHO concentration was 5 ppb, indicating VOCs at the observation site were abundant. In addition, similar to CO, peak HCHO concentration occurred around 8:00 LT, indicating the effect of anthropogenic emission-related sources~~Similar with CO, HCHO peaked around 8:00 LT with a maximum of 5 ppb, indicating the effect of anthropogenic emission-related sources. While the sampling site is located in a suburban area with no heavy traffic nearby, the maximum values of NO and NO_2 during the campaign reached 38.6 ppb and 49.6 ppb, respectively. The maximum diurnal averaged concentrations of NO and NO_2 were 4.4 ppb and 14.8 ppb, respectively. As VOC and NO_x are important precursors of O_3, relatively high NO_x and VOCs are conducive to O_3 production. The daily maximum 8-hour average O_3 concentrations~~O_3 concentrations throughout the observation period~~ frequently exceeded Class-II limit values (160 μg m^{-3}, which is equivalent to 82 ppb at 298 K and 1013 kpa) of the National Ambient Air Quality Standard, and the highest concentration can reach as high as 150 ppb, indicating serious photochemical pollution. From 6:00 LT, O_3 starts to rise rapidly with the increase in solar radiation intensity and reaches a maximum value of 85 ppb at 15:00 a.m. Subsequently, O_3 concentrations start to decrease rapidly due to the decrease in O_3 in-situ production, NO titration, and dry deposition. Concurrent $PM_{2.5}$ and O_3 pollution occurred from May 28 to 30, which is not unexpected as both pollutants are closely linked to the oxidation of VOCs and NO_x.

7

The co-occurrence of $PM_{2.5}$ and O_3 pollution in China has been frequently observed in recent years (Li et al., 2019b), especially in the spring and autumn seasons, making it a significant challenge for the next phase of air-cleaning actions in China to synergistically control both pollutants. OH radicals showed a typical diurnal pattern, with a maximum around noon and very low concentrations in the morning and night. The mean diurnal pattern shows that the average peak concentration of OH radicals is 1.0×10^7 cm^{-3}. With respect to summer OH concentrations in China, the average peak OH concentrations measured in this study are higher than that measured in ~~Shanghai (2.7×10^6 cm^{-3}) (Zhang et al., 2022a),~~ Wangdu (9.0×10^6 cm^{-3}) (Tan et al., 2017), Heshan (3.2×10^6 cm^{-3}) (Ma et al., 2022), Yufa (4.5×10^6 cm^{-3}) (Lu et al., 2013). The relatively high OH concentration implied strong atmospheric oxidizing capacity in this region. The reaction between OH and NO is the dominant gas-phase source of HONO. Compared with most other studies aiming at investigating the HONO budget, the concurrent measurement of OH radicals in our study will enable us to more accurately assess the contribution from other sources (excluding NO+OH) to HONO production.

HONO concentrations exhibited significant day-to-day variations, with the highest concentration reaching 4.4 ppb and the lowest concentration of several tens of ppt. The maximum HONO concentration was observed on the night of May 24, with HONO increasing from 1.8 ppb to 4.4 ppb in three hours. Interestingly, during this period, $PM_{2.5}$ increased concurrently from 112 μg m^{-3} to a maximum of 203 μg m^{-3}, indicating HONO and $PM_{2.5}$ might be originated from the same source. Considering HONO, $PM_{2.5}$, and CO increased concurrently in such a short period, a primary source like biomass burning was ~~possibly~~ the possible reason for this event.

In Figure ~~3~~2, HONO showed a typical diurnal pattern, i.e., high concentrations in the early morning and evening and low concentrations during the daytime, as typically observed at other rural, suburban, and urban sites (Li et al., 2010; Michoud et al., 2014; Xu et al., 2015; Lee et al., 2016). HONO generally began to accumulate in the evening, when HONO photolysis loss ceased. High NO_2 concentrations, which facilitated NO_2 heterogeneous reactions on humid surfaces, together with the primary vehicle emissions, led to an increase of HONO during the nighttime. After sunrise, HONO showed a rapid decrease due to fast photolysis and reached a minimum in the later afternoon. Considering that the atmospheric lifetime of HONO is only 10-20 min (with respect to photolysis) around noon (Sörgel et al., 2011), however, the averaged noon-time HONO concentration was relatively high (0.5 ppb), which implied the existence of strong daytime HONO sources to counteract its rapid photolysis. Furthermore, it can be clearly seen that periods with high NO_2 concentrations were typically accompanied by high HONO concentrations (May 29-30, June 5-7), and vice versa. This phenomenon further confirmed that NO_2 is an important precursor for HONO production. In addition, O_3 pollution episodes also coincided with high HONO levels (e.g., June 5-8). This phenomenon can be attributed to the following two reasons: firstly, O_3 and HONO have a common precursor NO_x; secondly, the photolysis of HONO will lead to the production of OH radicals, which will eventually promote the production of O_3, so the higher HONO

8

concentration will lead to the higher ~~concentration of~~ O_3 production, which will be further confirmed in our later model analysis.

HONO/NO_x is an important parameter to characterize the HONO concentration and the extent of NO_2 heterogeneous
240 conversion to HONO because it is less affected by transport and up-down convection compared to the HONO concentration. As shown in Figure ~~3~~2, HONO/NO_x started to increase after 18:30, when HONO photolysis loss ceased. However, with the fresh NO_x continuing to be emitted, the ratio then remains nearly constant overnight. The atmospheric lifetime of HONO is very short compared to NO_x. The main source of nocturnal HONO was generally considered to be the NO_2 heterogeneous hydrolysis reaction, and if this source also dominated daytime HONO
245 production, the rapid photolytic loss of HONO would make the daytime HONO/NO_x value decrease to a minimum. On the contrary, a daytime HONO/NO_x maximum (0.17) was observed around 12:00 LT, indicating other important sources, which is much faster than the NO_2 heterogeneous hydrolysis reaction, dominating daytime HONO production. Additionally, the mean diurnal pattern of HONO/NO_x resembled that of $j(O^1D)$, pointing to the possibility of light-promoted HONO sources being dominant during the day. In terms of mean diurnal profiles, the average peak value of
250 HONO/NO_x in this study is much larger than that reported in Beijing (0.08) (Gu et al., 2022), London (0.04) (Lee et al., 2016), and Nanjing (0.055) (Liu et al., 2019a) which indicated the high efficiency of NO_x to HONO conversion. HONO/NO_x measured in summer is typically higher than that measured in winter, which could be attributed to higher solar radiation intensity and hence promote the conversion of NO_x to HONO by photosensitized reduction. In addition, considering that the observation period covered the fertilization period in June, the high HONO/NO_x in our study may
255 be partially explained by direct HONO emissions around the sampling sites.

The average HONO concentration during the YRD-EXPLORE campaign is 0.62±0.49 ppb, which is within the range of the summer HONO concentration reported in previous studies, and is much lower than the observed concentration in winter in other sites in China, like Wangdu (1.8±1.4 ppb) (Xue et al., 2020), Xianghe (2.18±1.95 ppb) (Zhang et al., 2022b), Ji'nan (1.35 ppb) (Li et al., 2018a), and Beijing (0.98±0.85 ppb) (Zhang et al., 2022c), probably due to the
260 relatively low concentration of NO_x in summer. However, the observed HONO concentration is higher than that observed in summer in some suburban sites, like Hongkong (0.35±0.30 ppb) (Xu et al., 2015), Xi'an (0.51 ppb) (Huang et al., 2017), which also indicates the relatively high atmospheric oxidizing capacity in this region. Liu et al. (~~Liu et al.,~~ 2019a) reported a comparable summer HONO concentration of 0.56 ppb at a suburban site in the YRD region. Relatively high average HONO concentration of 0.76 ppb (0.01-5.95 ppb) was reported at a suburban site in
265 the YRD region during biomass burning season, which was attributed to the influence of biomass events (Nie et al., 2015).

3.2 HONO unknown source strength

More and more studies now confirm that gas-phase reactions are far from sufficient to explain the observed HONO concentrations, and in this study we also calculated the contribution of non-gas-phase reactions to the HONO

270 production based on the measured data ($P_{unknown}$). The reaction between NO and OH is the only considered gas-phase HONO source, and the removal pathways of HONO include photolysis, the reaction with OH radicals. Thus, $P_{unknown}$ is calculated as follows:

$$\frac{dHONO}{dt}=P_{NO+OH}+P_{unknown}-P_{HONO+OH}-P_{photolysis}$$

275 $$P_{unknown}=\frac{\Delta HONO}{\Delta t}+k_{HONO+OH}[HONO][OH]+j_{HONO}[HONO]-k_{NO+OH}[NO][OH]$$

dHONO/dt represents the change rate of observed HONO at 5-minute intervals. OH, NO, and j(HONO) were constrained by measured data. The reaction rate constants for NO+OH and HONO+OH were 9.8×10^{-12} cm^3 molecules^{-1} s^{-1} and 6.0×10^{-12} cm^3 molecules^{-1} s^{-1}, respectively. The calculated mean diurnal profile of $P_{unknown}$ is shown in Figure 4̶3. $P_{unknown}$ showed a symmetrical diurnal trend and peaked around 10:00-12:00 with a maximum of 2.5 ppb h^{-1}. The

280 variation of $P_{unknown}$ tracked the profile of j(O^{1}D), which may be a hint of a photo-induced process driving HONO production. The average peak value of $P_{unknown}$ was comparable to that measured in Beijing (2.58 ppb h^{-1}) and is larger than in Guangzhou (0.65 ppb h^{-1}), Santiago (1.77 ppb h^{-1}), indicating the important contribution of the unknown source to HONO production. While HONO concentration is relatively low at noon, the unknown source strength is the largest, as a strong source is needed to compensate for the rapid photolysis loss of HONO at noon.

285 Meanwhile, a 0-D box model was employed to understand the observed HONO profiles, and only the default NO+OH reaction was considered for HONO production (scenario S0 in Table 2). Although the HONO diurnal trend was captured in the base run simulation, the simulated HONO concentration was about an order of magnitude lower than the measured concentration (Figure 5̶4), further confirming the crucial role of non-gas-phase sources in HONO production. The simulated HONO concentration was less than 0.05 ppb around noontime, and the average peak

290 concentration was only 0.2 ppb.

3.3 Correlation analysis

As the unknown source strength of daytime HONO was much greater, we focused on analyzing the unknown source of daytime HONO in this part. According to our analysis above, photo-induced processes were likely to be the reason for the high observed HONO during the daytime. Previous studies have proposed some photo-induced heterogeneous

295 pathways, including photo-induced NO$_2$ to HONO conversion on the aerosol surface, photo-induced NO$_2$ to HONO

10

conversion on the ground surface, and heterogeneous nitrate photolysis. However, the relative importance of these sources to HONO production is still highly controversial. The comprehensive measurements performed during the EXPLORE-YRD campaign provide us with a unique opportunity to evaluate different HONO sources.

The correlation analysis between $P_{unknown}$ and other potential parameters can provide us with a preliminary understanding of the potential HONO sources. NO_2 concentration can be an important indicator of the heterogeneous reaction of NO_2 at the ground surface because the ground surface-to-volume ratio was considered to be constant for a well-mixed boundary layer. $NO_2 \times S_a$ can represent the heterogeneous NO_2 reaction on the aerosol surface. The particle nitrate concentration can be used as an indicator of nitrate photolysis. Therefore, $NO_2 \times j(NO_2)$, $NO_2 \times j(NO_2) \times S_a$, and $NO_3^- \times j(NO_2)$ can be used as proxies for three heterogeneous HONO sources, respectively. As shown in Figure 6̶5, we found that the unknown source correlated weakly with $NO_2 \times j(NO_2) \times S_a$, indicating photo-induced NO_2 conversion on the aerosol surface might play a minor role in daytime HONO production. In contrast, the correlation coefficients (R^2) of $P_{unknown}$ with $NO_2 \times j(NO_2)$ and $P_{unknown}$ with $NO_3^- \times j(NO_2)$ ($R^2=0.66$) were significantly higher, suggesting that the photo-induced NO_2 conversion on the ground surface and nitrate photolysis may have a profound impact on HONO production, which will be discussed in more detail in Section 3.4.

3.4 HONO formation by different heterogeneous mechanisms

In this section, sensitivity tests were performed to understand how the uncertainties of different photolytic HONO formation pathways would impact HONO production. The goal of these tests was to investigate if the potential HONO formation pathways could explain the profiles of $P_{unknown}$.

3.4.1 Photo-induced NO_2 conversion on the aerosol surface

The HONO production rate by photo-induced NO_2 conversion on the aerosol surface ($P_{aerosol+hv}$) can be expressed as follows:

$$P_{aerosol+hv} = \frac{1}{4} \gamma_{aerosol+hv} \times \frac{j(NO_2)}{0.005 \text{ s}^{-1}} \times [NO_2] \times \upsilon_{NO_2} \times S_a$$

Where υ_{NO2} is the mean molecule speed of NO_2, S_a is the aerosol surface area density̶a̶e̶r̶o̶s̶o̶l̶ ̶s̶u̶r̶f̶a̶c̶e̶ ̶t̶o̶ ̶v̶o̶l̶u̶m̶e̶ ̶r̶a̶t̶i̶o, and $\gamma_{aerosol+hv}$ is the photo-induced NO_2 uptake coefficient on the aerosol surface which depends on the solar radiation intensity. Previous laboratory studies have reported the positive dependence of $\gamma_{aerosol+hv}$ on solar radiation intensity. Accordingly, $\frac{j(NO_2)}{0.005 \text{ s}^{-1}}$ in the equation represents the promotion effect (Vogel et al., 2003; Wong et al., 2013).

From the equation, we can see that $\gamma_{aerosol+hv}$ is the key factor affecting the HONO production rate. The laboratory-derived $\gamma_{aerosol+hv}$ ranged from 10^{-4} to 10^{-7}, largely depending on the components of the model aerosols used in

11

laboratory experiments. $\gamma_{aeosol+hv}$ on the soot surface was measured to be 10^{-4} (Ammann et al., 1998) but rapidly decreased to 10^{-7} due to the consumption of reactive sites (Gerecke et al., 1998; Kleffmann et al., 1999). Stemmler et al. (~~Stemmler et al.,~~ 2007) measured $\gamma_{aeosol+hv}$ on the humic acid aerosol surface up to 2×10^{-5}, which was considered to be more relevant to ambient conditions. Here we used a photo-induced uptake coefficient of 2×10^{-5} and increased the value to 2×10^{-4} as an upper limit to check if the photo-induced NO_2 conversion on the aerosol surface could explain $P_{unknown}$. As shown in Figure ~~7a~~6a, HONO production by photo-induced NO_2 conversion on the aerosol surface was much lower than $P_{unknown}$ even with a $\gamma_{aeosol+hv}$ upper limit of 2×10^{-4}, indicating that the contribution of the photo-induced NO_2 conversion on the aerosol surface to HONO is minor, consistent with previous correlation analysis. A recent study also revealed NO_2 conversion on the aerosol surface contributed to less than 5% and 12% HONO production in the summer and winter seasons at a rural site, respectively (Song et al., 2022).

It should be mentioned that non-photo-induced NO_2 conversion (NO_2 hydrolysis) on the aerosol surface also contributed to HONO production during the daytime. However, NO_2 hydrolysis is generally considered to be much slower than photo-induced NO_2 conversion. Therefore, it couldn't be the main source of daytime HONO in our study and was not discussed here.

3.4.2 Heterogeneous nitrate photolysis

The expression for the contribution of heterogeneous nitrate photolysis to HONO production is as follows:

$$P_{NO_3^-+hv}=[NO_3^-]\times j(NO_3^-)=[NO_3^-]\times j(HNO_3)_g \times EF$$

Where $[NO_3^-]$ is the concentration of nitrate (ppb), $j(HNO_3)_g$ is the photolysis rate constant of gas-phase nitric acid, and EF is the enhancement factor (the ratio of aerosol-phase nitrate photolysis rate constant to gaseous nitrate photolysis rate constant). Recent evidence from a number of studies suggested that aerosol-phase nitrate photolyzes quickly to generate NO_2 or HONO with a rate between 10 and 300 times faster than that of gas-phase HNO_3 (Zhou et al., 2011; Ye et al., 2016; Ye et al., 2017). However, there is still great controversy about the rate constant of heterogeneous nitrate photolysis. For instance, observed NO_x and HNO_3 during the KORUS-AQ campaign were best explained with a moderate EF of 1-30 by detailed box modeling (Romer et al., 2018). Modeled O_3 would be largely overestimated compared to observations if EF was set to 120 in a recent modeling study, indicating EF under atmospherically relevant conditions may be much lower than 120 (Zhang et al., 2022a). Laufs et al. (~~Laufs and Kleffmann,~~ 2016) investigated HNO_3 photolysis on quartz glass surfaces and found EF value was less than 10. A recent chamber study indicated that suspended nitrate aerosol released HONO with an EF lower than 10 (Shi et al., 2021). Andersen et al. (~~Andersen et al.,~~ 2023) found the EF of marine nitrate aerosol increased with ~~relative humidity~~ RH and decreased with particulate nitrate concentrations by aircraft and ground measurements, which could partly explain the large discrepancy in EF values under different conditions.

12

355　We performed sensitivity tests with EF values of 20, 50, and 100 to understand how uncertainties in EF would impact HONO production and if particulate nitrate photolysis could explain $P_{unknown}$. As shown in Figure ~~7b~~6b, we calculated the HONO production rate of nitrate photolysis under different EF conditions and found that <u>regardless of </u>whether the EF is 20, 50, or 100, the calculated HONO production rate was about one order of magnitude lower than $P_{unknown}$, indicating that the contribution of nitrate photolysis to HONO is minor at this site due to relatively low concentration

360　of particulate nitrate in summer compared to winter. Zhang et al. (~~Zhang et al., ~~2022<u>a</u>~~b~~) pointed out that HONO production contributed by nitrate photolysis was a magnitude higher than that on clean days.

3.4.3 Photo-induced NO_2 conversion on the ground surface

Vertical HONO measurements revealed a negative profile (Kleffmann et al., 2003; Wong et al., 2013; Tuite et al., 2021), providing evidence that a strong HONO source is likely near the ground surface. Laboratory studies confirmed

365　the speculation and found that photo-induced reactions between NO_2 and organic material (e.g., humic acids) lead to pronounced HONO production (George et al., 2005; Stemmler et al., 2006; Han et al., 2016). Since humic acids are an important component of soil, and soil constitutes an important portion of the ground surface, this mechanism seems to be an important candidate for HONO sources in the lower troposphere.

HONO production by photo-induced NO_2 conversion on the ground surface can be expressed as follows:

370
$$P_{ground+hv} = \frac{1}{4}\gamma_{ground+hv} \times \frac{j(NO_2)}{0.005 \text{ s}^{-1}} \times [NO_2] \times \upsilon_{NO_2} \times \frac{1}{MLH}$$

According to laboratory-derived uptake coefficients on humic acids, $\gamma_{ground+hv}$ was on the order of 10^{-5} (Stemmler et al., 2006; Stemmler et al., 2007; Han et al., 2016), and sensitivity tests were performed with $\gamma_{ground+hv}$ of 2.5×10^{-5} and 4×10^{-5}. In addition, mixing layer height (MLH) was also a crucial factor influencing the HONO production rate on the ground surface. MLH refers to the height of the atmospheric layer where turbulent mixing occurs and pollutants are

375　effectively mixed throughout the layer. It is worth mentioning that MLH instead of boundary layer height (BLH) was used here, as BLH would result in a significant underestimation of surface HONO source strength. Recent HONO vertical measurements revealed HONO concentration at 100m was evidently lower than that near the surface, implying MLH was less than 100 m (Vogel et al., 2003; Vandenboer et al., 2013; Xing et al., 2021). Here we take the value of 50 m for the MLH based on previous studies (Lee et al., 2016; Xue et al., 2022; Zhang et al., 2022c). When the

380　$\gamma_{ground+hv}$ was 4×10^{-5}, the variation trend and magnitude of HONO production were similar to $P_{unknown}$ (Figure ~~7c~~6c), indicating photo-induced NO_2 conversion on the ground surface was an important HONO source. This was consistent with some studies combining field measurements and modeling simulations (Wong et al., 2013; Tuite et al., 2021).

3.5 HONO formation by vehicle emissions

It is generally accepted that HONO can be emitted by vehicle exhaust, and $HONO/NO_x$ is used as a proxy to quantify primary HONO emissions from vehicles. Based on previous studies (Kurtenbach et al., 2001; Liu et al., 2019a), we used a widely-applied ratio of 0.008 to calculate HONO emissions by vehicles at night. Considering the short lifetime of HONO with respect to photolysis during the daytime, the daytime HONO concentrations contributed by vehicles would be overestimated if a fixed value of $HONO/NO_x$ is used. Therefore, the atmospheric lifetime of NO_x and HONO should be taken into consideration to calculate vehicle emissions during the daytime (Xue et al., 2022; Zhang et al., 2022c).

Primary HONO emissions form vehicles can be expressed as follows:

$$HONO_{emi}=0.008 \times NO_x \quad \text{(nighttime)}$$

$$HONO_{emi}=0.008 \times NO_x \times \frac{\tau(HONO)}{\tau(NO_x)} \quad \text{(daytime)}$$

$\tau(HONO)$ and $\tau(NO_x)$ denotes the atmospheric lifetime of HONO and NO_x, respectively. $\tau(HONO)$ can be expressed as follows:

$$\tau(HONO)=\frac{1}{j(HONO)+OH \times k_{OH+HONO}}$$

NO_x in the atmosphere is mainly removed by reaction with OH to generate HNO_3 and N_2O_5 hydrolysis to generate HNO_3. N_2O_5 hydrolysis is negligible compared to NO_2+OH during the daytime. Therefore, the atmospheric lifetime of NO_x can be expressed as follows:

$$\tau(NO_x)=\frac{1}{OH \times k_{OH+NO_2}} \times \left(1+\frac{NO}{NO_2}\right)$$

The average diurnal profile of HONO contributed by vehicle emission is shown in Figure S2S3. The calculated contribution of vehicle emission to observed HONO ranged from 2% to 32%, with an average value of 15%.

3.6 Box modeling on HONO production with the incorporation of different HONO sources

Based on the above analysis, five heterogeneous HONO formation mechanisms were parameterized into the box model. The mechanisms and corresponding parameter settings are listed in Table 1. Such parameter settings are adopted from previous laboratory and modeling studies (Stemmler et al., 2006; Stemmler et al., 2007; Han et al., 2016; Romer et al., 2018; Zhang et al., 2022a).

As shown in Figure 87, included HONO sources significantly improved the model performance in HONO simulations. The box model incorporated with five heterogeneous sources (S1) well reproduced observed HONO profiles during nighttime, indicating a reasonable representation of nighttime HONO mechanisms. However, HONO concentration was still underestimated from 12:00 LT to 16:00 LT, which was likely caused by the following two reasons: i) the

14

uncertainty of $\gamma_{ground+hv}$, $\gamma_{aerosol+hv}$, and EF; ii) other unknown daytime sources of HONO that were not included in the model. Sensitivity tests were performed to see if the uncertainties of the parameters adopted in models caused the discrepancy between modeled and observed HONO concentrations during the daytime. The results of each sensitivity run were compared to that of S1, and the description of the changes in each sensitivity test is listed in Table 2. If we increased $\gamma_{ground+hv}$ to 6×10^{-5}, the HONO concentration from 12:00 LT to 15:00 LT could be explained, whereas the HONO concentration from 6:00 LT-12:00 LTwill be largely overestimated (S2 in Figure ~~9~~8); if we increased $\gamma_{aerosol+hv}$ to 2×10^{-4} (S3 in Figure ~~9~~8), the modeled daytime HONO nearly kept unchanged compared to S1 due to low aerosol surface to volume ratio; if we increased EF to 100, daytime HONO still couldn't be explained (S4 in Figure ~~9~~8), indicating underestimation of daytime HONO was not due to the uncertainties of $\gamma_{ground+hv}$, $\gamma_{aerosol+hv}$, and EF but was more likely due to other sources that were not considered. It should be noted that the box model can't take vertical transport into account, which may introduce additional uncertainty. Wong et al. (~~Wong et al.,~~ 2013) indicated that upward transport played an important role in distributing surface-produced HONO to the entire boundary layer. A 1D or 3D model may be an ideal tool for simulating HONO. The advantage of using the box model to explore the source of HONO was that the box model was constrained by simultaneously measured HONO precursors, which enabled a more accurate investigation of its secondary sources.

Modeled HONO profiles from May ~~28~~23 to June ~~12~~18 are shown in Figure ~~10~~9. Notably, simulated HONO profiles showed very good agreement with the observations from May ~~28~~23 to June 4, while underestimating daytime and nighttime HONO concentrations from June 5 to June ~~12~~16. Previous studies observed much higher HONO concentrations after fertilization compared to periods before fertilization (Xue et al., 2021). Given that the measurement site was surrounded by agricultural fields and the measurement period covered the fertilization event after the wheat harvest in June, fertilization event-induced soil HONO emissions may result in high daytime HONO levels and the HONO/NO$_x$ ratio. Thereby, field HONO flux measurements and laboratory investigations of corresponding mechanisms are warranted in future work to more accurately represent soil HONO emissions in models.

3.7 HONO budget

Figure ~~11a~~10a depicts the averaged diurnal profiles of the HONO production rates from six HONO sources (five heterogeneous sources and gas-phase NO+OH). During daytime (6:00-19:00), photo-induced NO$_2$ conversion on the ground surface was the main contributor to simulated HONO, accounting for ~~73~~71% of the total, followed by NO+OH ~~(10%)~~, NO$_2$ hydrolysis on the ground surface ~~(9%)~~, vehicle emission, photo-induced NO$_2$ conversion on the aerosol surface ~~(3%)~~, nitrate photolysis ~~(3%)~~, and NO$_2$ hydrolysis on the aerosol surface ~~(2%)~~. The maximum production rate by photo-induced NO$_2$ conversion on the ground surface was 1.85 ppb h^{-1}, which occurred around 9:00 LT. The NO+OH reaction played a minor role in HONO production. This is consistent with recent studies, which also revealed

that the NO+OH reaction was too small to explain daytime HONO (Li et al., 2018a; Michoud et al., 2014). In contrast, Liu et al. (~~Liu et al.,~~ 2021) reported that the NO+OH reaction dominated daytime HONO production in summer in Beijing, contributing 22% of total HONO production. Despite the uncertainties of $\gamma_{aerosol+hv}$ and EF, photo-induced NO_2 conversion on the aerosol surface and nitrate photolysis contributed to less than 10% of total production, implying they were not important in HONO production at this site. As suggested by previous studies, heterogeneous nitrate photolysis may be more important under low-NO_x conditions (Zhou et al., 2003; Elshorbany et al., 2012). NO_2 hydrolysis on the ground surface dominated HONO production during nighttime, contributing to 65% of total production, consistent with previous studies (Kleffmann et al., 2003; Vandenboer et al., 2013). HONO loss was dominated by photolysis, followed by deposition and reaction with OH (Figure ~~11b~~10b). The average peak loss rate by HONO photolysis was 2.3 ppb h^{-1}.

Despite a good match between observed and measured HONO during most days, HONO was still underestimated after fertilization events, indicating the strong influence of soil HONO emission on HONO budget in areas surrounded by agricultural fields. Therefore, soil HONO emission should be well constrained, especially for rural areas during fertilization periods. In addition, while nitrate photolysis played a negligible role in HONO formation in our study, it may play a more important role in winter polluted periods with high nitrate loadings. Our study highlighted important role of NO_2 conversion on ground surface. Previous studies found some coexisted gas species like NH_3, CO_2 may promote HONO production by NO_2 heterogeneous reaction (Li et al., 2018b; Xu et al., 2019; Liu et al., 2023a; Xia et al., 2021). Thereby, laboratory experiments investigating heterogeneous NO_2 conversion on ground surface with these species present are needed for better representation of HONO formation in models.

3.8 HONO contribution to RO_x and O_3 production

The primary sources of RO_x radicals mainly include O_3 photolysis, HONO photolysis, ozonolysis of alkenes, and carbonyl photolysis. Generally, in clean regions, O_3 photolysis is the main contributor to the primary source of radicals, while in polluted urban areas, HONO photolysis would exceed O_3 photolysis and become the main primary radical source. Field measurements revealed that HONO photolysis contributed to more than 40% of primary radical sources (Tan et al., 2017; Ma et al., 2019; Ren et al., 2006). Ozonolysis of alkenes is an important source of RO_x radicals at night. In addition, ozonolysis of alkenes was the second largest radical source during the winter in urban areas (Tan et al., 2018). During the winter in oil- and natural gas-producing basins in the United States, carbonyl photolysis was found to be the largest radical source, initiating the photochemical chain reactions and ultimately leading to exceedances of O_3 concentration (Edwards et al., 2014). Similarly, carbonyl photolysis was the major primary source of radicals in the oil extraction region in China during the winter seasons (Chen et al., 2020).

Figure ~~12~~ 11 depicts the contribution of different channels to the primary source of RO_x in the Taizhou area. We can
clearly see that HONO photolysis is the dominant contributor to the primary source of RO_x, not only in the early
morning but also throughout the day. HONO photolysis contributed to 43% of RO_x production during the daytime,
followed by O_3 photolysis (17%), HCHO photolysis (14%), ozonolysis of alkenes (12%), and carbonyl photolysis
(10%). The maximum RO_x production rate by HONO photolysis was 2.6 ppb h^{-1}, which occurs around 11:00 LT.
HONO photolysis was also identified as the major source of primary RO_x production in the summer of Chengdu (34%),
and Wangdu (38%) (Tan et al., 2017; Yang et al., 2021b). The results above indicate that HONO is closely linked to
the RO_x budget, and it is crucial to accurately identify HONO sources in order to fully comprehend the atmospheric
oxidation capacity.

As mentioned in Section 3.1, O_3 episodes were typically accompanied by high HONO levels. In this section, a box
model was employed to quantify the contribution of HONO to O_3 production. $F(O_3)$ and $P(O_3)$ was first calculated
with observed HONO as constraint. $F(O_3)$ showed a typical diurnal pattern with a maximum of 15.8 ppb h^{-1} occurring
around 9:00 LT (Figure ~~13~~12). When observed HONO was not constrained in the model, the average peak of $F(O_3)$
decreased nearly 45% to 8.8 ppb h^{-1} (Figure ~~13~~12), indicating HONO significantly contributed to O_3 production and
thereby boosted O_3 pollution during the summer. $P(O_3)$ decreased from 12.6 ppb h^{-1} to 6.7 ppb h^{-1} with a 47%
reduction, which is higher than the 20% reduction in urban Beijing (Li et al., 2021; Zhang et al., 2023). Yang et al.
(~~Yang et al.,~~ 2021c) observed two O_3 pollution episodes with nearly identical O_3 precursor (VOC and NO_x) levels.
Interestingly, they found higher O_3 peak concentrations coinciding with higher HONO concentrations in one of the
episodes. This correlation can be attributed to the fact that higher HONO concentrations can lead to higher levels of
OH radicals, which can, in turn, enhance the production of O_3 by initiating the chain reactions (Yang et al., 2021c). We
also modeled OH radicals with and without observed HONO as a model constraint. The modeled OH averaged peak
concentration with HONO was 8×10^6 cm^{-3}, which was nearly twice as high as that (4.4×10^6 cm^{-3}) without HONO as a
model constraint. Our results emphasized the importance of HONO in primary radical production and O_3 production.
Accurately representing HONO sources in models is crucial for characterizing atmospheric oxidation capacity and
quantifying secondary pollutants production. Therefore, more field, laboratory, and modeling studies are urgently
needed to develop more concise HONO formation parameterizations. In addition, more and more studies are focusing
on VOCs and NO_x reduction to achieve O_3 mitigation. However, O_3 formation showed non-linear relationship on
VOCs and NO_x, making it difficult to decrease O_3 by solely reducing VOCs or NO_x. For instance, during COVID-19
lockdown period, O_3 showed an evident increase while NO_x and VOCs showed a decrease trend, highlight the
complexity of O_3 mitigation (Zhao et al., 2020; Wang et al., 2022). Our results suggested HONO contributed
significantly to O_3 production in China, and thereby, reducing HONO production may be an alternative way for O_3
control. As NO_2 heterogeneous reactions on the ground surface were important sources for HONO production,

17

reducing NO_x emissions would be beneficial for reducing HONO emissions. However, NO_x reduction may also lead to more O_3 production if O_3 formation is in a VOC-limited regime, and hence the overall effects of NO_x reduction on O_3 should be evaluated by chemical transport models. Moreover, soil HONO emissions may become an important source in rural area with large areas of agricultural fields. Decreasing soil HONO emissions is beneficial for O_3 pollution control, especially during fertilization period in June when the O_3 pollution was severe. Therefore, more environmental-friendly fertilization amount and fertilization mode should be investigated to decrease soil HONO emissions.

4. Conclusions

HONO measurements, along with a wide range of gas-phase, aerosol-phase, and meteorological measurements, were conducted during the EXPLORE-YRD campaign. HONO concentrations exhibited significant day-to-day variations, with the highest concentration reaching 4.4 ppb and the lowest concentration of several tens of ppt. The relatively higher summer HONO and OH concentrations compared to other suburban sites suggested higher atmospheric oxidation capacity. $HONO/NO_x$ exhibited a diurnal pattern similar to $j(O^1D)$, with a maximum of 0.17 around noon, implying the existence of photo-induced HONO sources. The box model with the only default HONO source (OH+NO) failed to capture the observed HONO concentration. The calculated $P_{unknown}$ showed a diurnal pattern with a maximum of 2.5 ppb h^{-1} occurring around 10:00-12:00 LT. The correlation coefficients of $P_{unknown}$ with $NO_2 \times j(NO_2)$ and $NO_3^- \times j(NO_2)$ were significantly higher than that of $P_{unknown}$ with $NO_2 \times j(NO_2) \times S_a$, indicating photo-induced NO_2 conversion on the aerosol surface played a minor role in HONO production. Sensitivity tests suggested HONO production rate by photo-induced NO_2 conversion on the ground surface was able to explain $P_{unknown}$. With additional HONO sources incorporated, the box well reproduced the nighttime HONO concentration but still underestimated the daytime HONO concentration. Further sensitivity tests implied the discrepancy between modeled and observed daytime HONO concentration was not due to uncertainties in $\gamma_{ground+hv}$, $\gamma_{aerosol+hv}$, and EF but was more likely due to other HONO sources that were not considered. Among the heterogeneous and gas-phase HONO sources, photo-induced NO_2 conversion on the ground surface was the main contributor to simulated daytime HONO, accounting for 73% of the total, followed by NO+OH (10%), NO_2 hydrolysis on the ground surface (9%), photo-induced NO_2 conversion on the aerosol surface (3%), nitrate photolysis (3%), and NO_2 hydrolysis on the aerosol surface (2%). The maximum production rate of photo-induced NO_2 conversion on the ground surface was 1.85 ppb h^{-1} which occurred around 9:00 LT. NO_2 hydrolysis on the ground surface was the major source of nighttime HONO, contributing to 65% of total HONO production. HONO loss was dominated by photolysis, followed by deposition and reaction with OH.

18

HONO photolysis contributed to 43% of RO_x production during the daytime, followed by O_3 photolysis (17%), HCHO photolysis (14%), ozonolysis of alkenes (12%), and carbonyl photolysis (10%). The maximum RO_x production rate by HONO photolysis was 2.6 ppb h^{-1}, which occurs around 11:00 LT. When the observed HONO was not constrained in the box model, the calculated $P(O_3)$ showed a typical diurnal pattern with a maximum of ~~12.6~~6.7 ppb h^{-1} occurring around 9:00 LT. $P(O_3)$ would ~~decrease~~ increase by ~~45~~88% to ~~6.7~~12.6 ppb h^{-1} if HONO was not constrained, indicating HONO significantly enhanced O_3 production and hence aggravated O_3 pollution during the summer season.

19

References

Alicke, B., Geyer, A., Hofzumahaus, A., Holland, F., Konrad, S., Pätz, H. W., Schäfer, J., Stutz, J., Volz-Thomas, A., and Platt, U.: OH formation by HONO photolysis during the BERLIOZ experiment, Journal of Geophysical Research: Atmospheres, 108, PHO 3-1-PHO 3-17, https://doi.org/10.1029/2001JD000579, 2003.

Ammann, M., Kalberer, M., Jost, D. T., Tobler, L., Rossler, E., Piguet, D., Gaggeler, H. W., and Baltensperger, U.: Heterogeneous production of nitrous acid on soot in polluted air masses, Nature, 395, 157-160, 10.1038/25965, 1998.

Andersen, S. T., Carpenter, L. J., Reed, C., Lee, J. D., Chance, R., Sherwen, T., Vaughan, A. R., Stewart, J., Edwards, P. M.,Bloss, W. J., Sommariva, R., Crilley, L. R., Nott, G. J., Neves, L., Read, K., Heard, D. E., Seakins, P. W., Whalley, L. K., Boustead, G. A., Fleming, L. T., Stone, D., and Fomba, K. W.: Extensive field evidence for the release of HONO from the photolysis of nitrate aerosols, Sci Adv, 9, eadd6266, 10.1126/sciadv.add6266, 2023.

Baergen, A. M. and Donaldson, D. J.: Photochemical Renoxification of Nitric Acid on Real Urban Grime, Environ Sci Technol, 47, 815-820, 10.1021/es3037862, 2013.

Bao, F. X., Li, M., Zhang, Y., Chen, C. C., and Zhao, J. C.: Photochemical Aging of Beijing Urban PM2.5: HONO Production, Environ Sci Technol, 52, 6309-6316, 2018
.
Bejan, I., Abd El Aal, Y., Barnes, I., Benter, T., Bohn, B., Wiesen, P., and Kleffmann, J.: The photolysis of ortho-nitrophenols: a new gas phase source of HONO, Phys Chem Chem Phys, 8, 2028-2035, 10.1039/b516590c, 2006.

Chen, T., Xue, L., Zheng, P., Zhang, Y., Liu, Y., Sun, J., Han, G., Li, H., Zhang, X., Li, Y., Li, H., Dong, C., Xu, F., Zhang, Q., and Wang, W.: Volatile organic compounds and ozone air pollution in an oil production region in northern China, Atmos. Chem. Phys., 20, 7069-7086, 10.5194/acp-20-7069-2020, 2020.

Cui, L. L., Li, R., Fu, H. B., Meng, Y., Zhao, Y. L., Li, Q., and Chen, J. M.: Nitrous acid emission from open burning of major crop residues in mainland China, Atmos Environ, 244, 10, 10.1016/j.atmosenv.2020.117950, 2021.

Ding, A. J., Fu, C. B., Yang, X. Q., Sun, J. N., Zheng, L. F., Xie, Y. N., Herrmann, E., Nie, W., Petaja, T., Kerminen, V. M.,and Kulmala, M.: Ozone and fine particle in the western Yangtze River Delta: an overview of 1 yr data at the SORPES station, Atmos Chem Phys, 13, 5813-5830, 10.5194/acp-13-5813-2013, 2013.

Edwards, P. M., Brown, S. S., Roberts, J. M., Ahmadov, R., Banta, R. M., deGouw, J. A., Dube, W. P., Field, R. A., Flynn, J. H., Gilman, J. B., Graus, M., Helmig, D., Koss, A., Langford, A. O., Lefer, B. L., Lerner, B. M., Li, R., Li, S. M., McKeen, S. A., Murphy, S. M., Parrish, D. D., Senff, C. J., Soltis, J., Stutz, J., Sweeney, C., Thompson, C. R., Trainer, M. K., Tsai, C., Veres, P. R., Washenfelder, R. A., Warneke, C., Wild, R. J., Young, C. J., Yuan, B., and Zamora, R.: High winter ozone pollution from carbonyl photolysis in an oil and gas basin, Nature, 514, 351-354, 10.1038/nature13767, 2014.

Elshorbany, Y. F., Steil, B., Bruhl, C., and Lelieveld, J.: Impact of HONO on global atmospheric chemistry calculated with an empirical parameterization in the EMAC model, Atmos Chem Phys, 12, 9977-10000, 10.5194/acp-12-9977-2012, 2012.

Elshorbany, Y. F., Kurtenbach, R., Wiesen, P., Lissi, E., Rubio, M., Villena, G., Gramsch, E., Rickard, A. R., Pilling, M. J., and Kleffmann, J.: Oxidation capacity of the city air of Santiago, Chile, Atmos Chem Phys, 9, 2257-2273, 10.5194/acp-9-2257-2009, 2009.

Finlayson-Pitts, B. J., Wingen, L. M., Sumner, A. L., Syomin, D., and Ramazan, K. A.: The heterogeneous hydrolysis of NO2 in laboratory systems and in outdoor and indoor atmospheres: An integrated mechanism, Phys Chem Chem Phys, 5, 223-242, 2003.

20

Fu, X., Wang, T., Zhang, L., Li, Q. Y., Wang, Z., Xia, M., Yun, H., Wang, W. H., Yu, C., Yue, D. L., Zhou, Y., Zheng, J. Y., and Han, R.: The significant contribution of HONO to secondary pollutants during a severe winter pollution event in southern China, Atmos Chem Phys, 19, 1-14, 10.5194/acp-19-1-2019, 2019.

George, C., Strekowski, R. S., Kleffmann, J., Stemmler, K., and Ammann, M.: Photoenhanced uptake of gaseous NO2 on solid organic compounds: a photochemical source of HONO?, Faraday Discussions, 130, 195-210, 10.1039/B417888M, 2005.

Gerecke, A., Thielmann, A., Gutzwiller, L., and Rossi, M. J.: The chemical kinetics of HONO formation resulting from heterogeneous interaction of NO2 with flame soot, Geophys Res Lett, 25, 2453-2456, 10.1029/98gl01796, 1998.

Gu, R. R., Shen, H. Q., Xue, L. K., Wang, T., Gao, J., Li, H., Liang, Y. T., Xia, M., Yu, C., Liu, Y. M., and Wang, W. X.: Investigating the sources of atmospheric nitrous acid (HONO) in the megacity of Beijing, China, Sci Total Environ, 812, 10, 10.1016/j.scitotenv.2021.152270, 2022.

Han, C., Yang, W. J., Wu, Q. Q., Yang, H., and Xue, X. X.: Heterogeneous Photochemical Conversion of NO2 to HONO on the Humic Acid Surface under Simulated Sunlight, Environ Sci Technol, 50, 5017-5023, 10.1021/acs.est.5b05101, 2016.
Heland, J., Kleffmann, J., Kurtenbach, R., and Wiesen, P.: A New Instrument To Measure Gaseous Nitrous Acid (HONO) in the Atmosphere, Environ Sci Technol, 35, 3207-3212, 10.1021/es000303t, 2001.

Hou, S., Tong, S., Ge, M., and An, J.: Comparison of atmospheric nitrous acid during severe haze and clean periods in Beijing, China, Atmos Environ, 124, 199-206, https://doi.org/10.1016/j.atmosenv.2015.06.023, 2016.

Huang, R. J., Yang, L., Cao, J. J., Wang, Q. Y., Tie, X. X., Ho, K. F., Shen, Z. X., Zhang, R. J., Li, G. H., Zhu, C. S., Zhang, N. N., Dai, W. T., Zhou, J. M., Liu, S. X., Chen, Y., Chen, J., and O'Dowd, C. D.: Concentration and sources of atmospheric nitrous acid (HONO) at an urban site in Western China, Sci Total Environ, 593, 165-172, 10.1016/j.scitotenv.2017.02.166, 2017.

Kleffmann, J., Becker, K. H., Lackhoff, M., and Wiesen, P.: Heterogeneous conversion of NO2 on carbonaceous surfaces, Phys Chem Chem Phys, 1, 5443-5450, 10.1039/a905545b, 1999.

Kleffmann, J., Kurtenbach, R., Lörzer, J., Wiesen, P., Kalthoff, N., Vogel, B., and Vogel, H.: Measured and simulated vertical profiles of nitrous acid—Part I: Field measurements, Atmos Environ, 37, 2949-2955, https://doi.org/10.1016/S1352-2310(03)00242-5, 2003.

Kleffmann, J., Gavriloaiei, T., Hofzumahaus, A., Holland, F., Koppmann, R., Rupp, L., Schlosser, E., Siese, M., and Wahner, A.: Daytime formation of nitrous acid: A major source of OH radicals in a forest, Geophys Res Lett, 32, https://doi.org/10.1029/2005GL022524, 2005.

Kramer, L. J., Crilley, L. R., Adams, T. J., Ball, S. M., Pope, F. D., and Bloss, W. J.: Nitrous acid (HONO) emissions under real-world driving conditions from vehicles in a UK road tunnel, Atmos. Chem. Phys., 20, 5231-5248, 10.5194/acp-20-5231-2020, 2020.

Kurtenbach, R., Becker, K. H., Gomes, J. A. G., Kleffmann, J., Lörzer, J. C., Spittler, M., Wiesen, P., Ackermann, R., Geyer, A., and Platt, U.: Investigations of emissions and heterogeneous formation of HONO in a road traffic tunnel, Atmos Environ, 35, 3385-3394, https://doi.org/10.1016/S1352-2310(01)00138-8, 2001.

Laufs, S. and Kleffmann, J.: Investigations on HONO formation from photolysis of adsorbed HNO3 on quartz glass surfaces, Phys Chem Chem Phys, 18, 9616-9625, 10.1039/C6CP00436A, 2016.

Lee, J. D., Whalley, L. K., Heard, D. E., Stone, D., Dunmore, R. E., Hamilton, J. F., Young, D. E., Allan, J. D., Laufs, S., and Kleffmann, J.: Detailed budget analysis of HONO in central London reveals a missing daytime source, Atmos Chem Phys, 16, 2747-2764, 10.5194/acp-16-2747-2016, 2016.

665 Li, D. D., Xue, L. K., Wen, L., Wang, X. F., Chen, T. S., Mellouki, A., Chen, J. M., and Wang, W. X.: Characteristics and sources of nitrous acid in an urban atmosphere of northern China: Results from 1-yr continuous observations, Atmos Environ, 182, 296-306, 10.1016/j.atmosenv.2018.03.033, 2018a.

Li, G., Lei, W., Zavala, M., Volkamer, R., Dusanter, S., Stevens, P., and Molina, L. T.: Impacts of HONO sources on the
670 photochemistry in Mexico City during the MCMA-2006/MILAGO Campaign, Atmos Chem Phys, 10, 6551-6567, 10.5194/acp-10-6551-2010, 2010.

Li, K., Jacob, D. J., Liao, H., Shen, L., Zhang, Q., and Bates, K. H.: Anthropogenic drivers of 2013-2017 trends in summer surface ozone in China, P Natl Acad Sci USA, 116, 422-427, 10.1073/pnas.1812168116, 2019a.
675
Li, K., Jacob, D. J., Liao, H., Zhu, J., Shah, V., Shen, L., Bates, K. H., Zhang, Q., and Zhai, S. X.: A two-pollutant strategy for improving ozone and particulate air quality in China, Nat Geosci, 12, 906-910, 10.1038/s41561-019-0464-x, 2019b.

Li, L., Duan, Z. Y., Li, H., Zhu, C. Q., Henkelman, G., Francisco, J. S., and Zeng, X. C.: Formation of HONO from the
680 NH3-promoted hydrolysis of NO2 dimers in the atmosphere, P Natl Acad Sci USA, 115, 7236-7241, 10.1073/pnas.1807719115, 2018b.

Li, Q. Y., Zhang, L., Wang, T., Wang, Z., Fu, X., and Zhang, Q.: "New" Reactive Nitrogen Chemistry Reshapes the Relationship of Ozone to Its Precursors, Environ Sci Technol, 52, 2810-2818, 10.1021/acs.est.7b05771, 2018b2018c.
685
Li, S. P., Matthews, J., and Sinha, A.: Atmospheric hydroxyl radical production from electronically excited NO2 and H2O, Science, 319, 1657-1660, 10.1126/science.1151443, 2008.

Li, Y., Wang, X., Wu, Z., Li, L., Wang, C., Li, H., Zhang, X., Zhang, Y., Li, J., Gao, R., Xue, L., Mellouki, A., Ren, Y., and
690 Zhang, Q.: Atmospheric nitrous acid (HONO) in an alternate process of haze pollution and ozone pollution in urban Beijing in summertime: Variations, sources and contribution to atmospheric photochemistry, Atmospheric Research, 260, 105689, https://doi.org/10.1016/j.atmosres.2021.105689, 2021.

Liu, J., Li, B., Deng, H., Yang, Y., Song, W., Wang, X., Luo, Y., Francisco, J. S., Li, L., and Gligorovski, S.: Resolving the
695 Formation Mechanism of HONO via Ammonia-Promoted Photosensitized Conversion of Monomeric NO2 on Urban Glass Surfaces, Journal of the American Chemical Society, 145, 11488-11493, 10.1021/jacs.3c02067, 2023a.

Liu, J. Y., Liu, Z. R., Ma, Z. Q., Yang, S. H., Yao, D., Zhao, S. M., Hu, B., Tang, G. Q., Sun, J., Cheng, M. T., Xu, Z. J., and Wang, Y. S.: Detailed budget analysis of HONO in Beijing, China: Implication on atmosphere oxidation capacity in polluted
700 megacity, Atmos Environ, 244, 14, 10.1016/j.atmosenv.2020.117957, 2021.

Liu, P., Xue, C., Ye, C., Liu, C., Zhang, C., Wang, J., Zhang, Y., Liu, J., and Mu, Y.: The Lack of HONO Measurement May Affect the Accurate Diagnosis of Ozone Production Sensitivity, ACS Environmental Au, 3, 18-23, 10.1021/acsenvironau.2c00048, 2023b.
705
Liu, Y., Nie, W., Xu, Z., Wang, T., Wang, R., Li, Y., Wang, L., Chi, X., and Ding, A.: Semi-quantitative understanding of source contribution to nitrous acid (HONO) based on 1 year of continuous observation at the SORPES station in eastern China, Atmos. Chem. Phys., 19, 13289-13308, 10.5194/acp-19-13289-2019, 2019a.

22

710 Liu, Y., Zhao, Q., Hao, X., Zhao, J., Zhang, Y., Yang, X., Fu, Q., Xu, X., Wang, X., Huo, J., and Chen, J.: Increasing surface ozone and enhanced secondary organic carbon formation at a city junction site: An epitome of the Yangtze River Delta, China (2014–2017), Environ Pollut, 265, 114847, https://doi.org/10.1016/j.envpol.2020.114847, 2020.

Liu, Y., Lu, K., Li, X., Dong, H., Tan, Z., Wang, H., Zou, Q., Wu, Y., Zeng, L., Hu, M., Min, K.-E., Kecorius, S.,
715 Wiedensohler, A., and Zhang, Y.: A Comprehensive Model Test of the HONO Sources Constrained to Field Measurements at Rural North China Plain, Environ Sci Technol, 53, 3517-3525, 10.1021/acs.est.8b06367, 2019b.

Lu, K. D., Hofzumahaus, A., Holland, F., Bohn, B., Brauers, T., Fuchs, H., Hu, M., Häseler, R., Kita, K., Kondo, Y., Li, X., Lou, S. R., Oebel, A., Shao, M., Zeng, L. M., Wahner, A., Zhu, T., Zhang, Y. H., and Rohrer, F.: Missing OH source in a
720 suburban environment near Beijing: observed and modelled OH and HO2 concentrations in summer 2006, Atmos. Chem. Phys., 13, 1057-1080, 10.5194/acp-13-1057-2013, 2013.

Ma, X. F., Tan, Z. F., Lu, K. D., Yang, X. P., Liu, Y. H., Li, S. L., Li, X., Chen, S. Y., Novelli, A., Cho, C. M., Zeng, L. M., Wahner, A., and Zhang, Y. H.: Winter photochemistry in Beijing: Observation and model simulation of OH and HO2
725 radicals at an urban site, Sci Total Environ, 685, 85-95, 2019.

Ma, X. F., Tan, Z. F., Lu, K. D., Yang, X. P., Chen, X. R., Wang, H. C., Chen, S. Y., Fang, X., Li, S. L., Li, X., Liu, J. W., Liu, Y., Lou, S. R., Qiu, W. Y., Wang, H. L., Zeng, L. M., and Zhang, Y. H.: OH and HO2 radical chemistry at a suburban site during the EXPLORE-YRD campaign in 2018, Atmos Chem Phys, 22, 7005-7028, 10.5194/acp-22-7005-2022, 2022.
730

Michoud, V., Colomb, A., Borbon, A., Miet, K., Beekmann, M., Camredon, M., Aumont, B., Perrier, S., Zapf, P., Siour, G., Ait-Helal, W., Afif, C., Kukui, A., Furger, M., Dupont, J. C., Haeffelin, M., and Doussin, J. F.: Study of the unknown HONO daytime source at a European suburban site during the MEGAPOLI summer and winter field campaigns, Atmos Chem Phys, 14, 2805-2822, 10.5194/acp-14-2805-2014, 2014.
735

Michoud, V., Kukui, A., Camredon, M., Colomb, A., Borbon, A., Miet, K., Aumont, B., Beekmann, M., Durand-Jolibois, R., Perrier, S., Zapf, P., Siour, G., Ait-Helal, W., Locoge, N., Sauvage, S., Afif, C., Gros, V., Furger, M., Ancellet, G., and Doussin, J. F.: Radical budget analysis in a suburban European site during the MEGAPOLI summer field campaign, Atmos. Chem. Phys., 12, 11951-11974, 10.5194/acp-12-11951-2012, 2012.
740

Neftel, A., Blatter, A., Hesterberg, R., and Staffelbach, T.: Measurements of concentration gradients of HNO2 and HNO3 over a semi-natural ecosystem, Atmos Environ, 30, 3017-3025, https://doi.org/10.1016/1352-2310(96)00011-8, 1996.

Nie, W., Ding, A. J., Xie, Y. N., Xu, Z., Mao, H., Kerminen, V. M., Zheng, L. F., Qi, X. M., Huang, X., Yang, X. Q., Sun, J.
745 N., Herrmann, E., Petaja, T., Kulmala, M., and Fu, C. B.: Influence of biomass burning plumes on HONO chemistry in eastern China, Atmos Chem Phys, 15, 1147-1159, 10.5194/acp-15-1147-2015, 2015.

Oswald, R., Behrendt, T., Ermel, M., Wu, D., Su, H., Cheng, Y., Breuninger, C., Moravek, A., Mougin, E., Delon, C., Loubet, B., Pommerening-Roser, A., Sorgel, M., Poschl, U., Hoffmann, T., Andreae, M. O., Meixner, F. X., and Trebs, I.:
750 HONO Emissions from Soil Bacteria as a Major Source of Atmospheric Reactive Nitrogen, Science, 341, 1233-1235, 10.1126/science.1242266, 2013.

Ren, X., Brune, W. H., Mao, J., Mitchell, M. J., Lesher, R. L., Simpas, J. B., Metcalf, A. R., Schwab, J. J., Cai, C., and Li, Y.: Behavior of OH and HO2 in the winter atmosphere in New York City, Atmos Environ, 40, 252-263,
755 10.1016/j.atmosenv.2005.11.073, 2006.

Ren, X. R., Harder, H., Martinez, M., Lesher, R. L., Oliger, A., Simpas, J. B., Brune, W. H., Schwab, J. J., Demerjian, K. L., He, Y., Zhou, X. L., and Gao, H. G.: OH and HO2 chemistry in the urban atmosphere of New York City, Atmos Environ, 37, 3639-3651, 10.1016/s1352-2310(03)00459-x, 2003.

760

Romer, P. S., Wooldridge, P. J., Crounse, J. D., Kim, M. J., Wennberg, P. O., Dibb, J. E., Scheuer, E., Blake, D. R., Meinardi, S., Brosius, A. L., Thames, A. B., Miller, D. O., Brune, W. H., Hall, S. R., Ryerson, T. B., and Cohen, R. C.: Constraints on Aerosol Nitrate Photolysis as a Potential Source of HONO and NOx, Environ Sci Technol, 52, 13738-13746, 2018.

765

Scharko, N. K., Schütte, U. M. E., Berke, A. E., Banina, L., Peel, H. R., Donaldson, M. A., Hemmerich, C., White, J. R., and Raff, J. D.: Combined Flux Chamber and Genomics Approach Links Nitrous Acid Emissions to Ammonia Oxidizing Bacteria and Archaea in Urban and Agricultural Soil, Environ Sci Technol, 49, 13825-13834, 10.1021/acs.est.5b00838, 2015.

770

Shi, Q., Tao, Y., Krechmer, J. E., Heald, C. L., Murphy, J. G., Kroll, J. H., and Ye, Q.: Laboratory Investigation of Renoxification from the Photolysis of Inorganic Particulate Nitrate, Environ Sci Technol, 55, 854-861, 2021.

Song, Y., Zhang, Y., Xue, C., Liu, P., He, X., Li, X., and Mu, Y.: The seasonal variations and potential sources of nitrous acid (HONO) in the rural North China Plain, Environ Pollut, 311, 119967, https://doi.org/10.1016/j.envpol.2022.119967, 775   2022.

Sorgel, M., Regelin, E., Bozem, H., Diesch, J. M., Drewnick, F., Fischer, H., Harder, H., Held, A., Hosaynali-Beygi, Z., Martinez, M., and Zetzsch, C.: Quantification of the unknown HONO daytime source and its relation to NO2, Atmos Chem Phys, 11, 10433-10447, 10.5194/acp-11-10433-2011, 2011.

780

Spataro, F., Ianniello, A., Esposito, G., Allegrini, I., Zhu, T., and Hu, M.: Occurrence of atmospheric nitrous acid in the urban area of Beijing (China), Sci Total Environ, 447, 210-224, 10.1016/j.scitotenv.2012.12.065, 2013.

Stemmler, K., Ammann, M., Donders, C., Kleffmann, J., and George, C.: Photosensitized reduction of nitrogen dioxide on 785   humic acid as a source of nitrous acid, Nature, 440, 195-198, 10.1038/nature04603, 2006.

Stemmler, K., Ndour, M., Elshorbany, Y., Kleffmann, J., D'Anna, B., George, C., Bohn, B., and Ammann, M.: Light induced conversion of nitrogen dioxide into nitrous acid on submicron humic acid aerosol, Atmos Chem Phys, 7, 4237-4248, 10.5194/acp-7-4237-2007, 2007.

790

Stutz, J., Alicke, B., Ackermann, R., Geyer, A., Wang, S. H., White, A. B., Williams, E. J., Spicer, C. W., and Fast, J. D.: Relative humidity dependence of HONO chemistry in urban areas, J Geophys Res-Atmos, 109, 14, 10.1029/2003jd004135, 2004.

795   Su, H., Cheng, Y. F., Oswald, R., Behrendt, T., Trebs, I., Meixner, F. X., Andreae, M. O., Cheng, P., Zhang, Y., and Poschl, U.: Soil Nitrite as a Source of Atmospheric HONO and OH Radicals, Science, 333, 1616-1618, 2011.

Tan, Z., Rohrer, F., Lu, K., Ma, X., Bohn, B., Broch, S., Dong, H., Fuchs, H., Gkatzelis, G. I., Hofzumahaus, A., Holland, F., Li, X., Liu, Y., Liu, Y., Novelli, A., Shao, M., Wang, H., Wu, Y., Zeng, L., Hu, M., Kiendler-Scharr, A., Wahner, A., and 800   Zhang, Y.: Wintertime photochemistry in Beijing: observations of ROx radical concentrations in the North China Plain during the BEST-ONE campaign, Atmos. Chem. Phys., 18, 12391-12411, 10.5194/acp-18-12391-2018, 2018.

Tan, Z. F., Fuchs, H., Lu, K. D., Hofzumahaus, A., Bohn, B., Broch, S., Dong, H. B., Gomm, S., Haseler, R., He, L. Y., Holland, F., Li, X., Liu, Y., Lu, S. H., Rohrer, F., Shao, M., Wang, B. L., Wang, M., Wu, Y. S., Zeng, L. M., Zhang, Y. S., 805   Wahner, A., and Zhang, Y. H.: Radical chemistry at a rural site (Wangdu) in the North China Plain: observation and model calculations of OH, HO2 and RO2 radicals, Atmos Chem Phys, 17, 663-690, 10.5194/acp-17-663-2017, 2017.

Theys, N., Volkamer, R., Müller, J. F., Zarzana, K. J., Kille, N., Clarisse, L., De Smedt, I., Lerot, C., Finkenzeller, H., Hendrick, F., Koenig, T. K., Lee, C. F., Knote, C., Yu, H., and Van Roozendael, M.: Global nitrous acid emissions and levels of regional oxidants enhanced by wildfires, Nat Geosci, 13, 681-686, 10.1038/s41561-020-0637-7, 2020.

Tuite, K., Thomas, J. L., Veres, P. R., Roberts, J. M., Stevens, P. S., Griffith, S. M., Dusanter, S., Flynn, J. H., Ahmed, S., Emmons, L., Kim, S.-W., Washenfelder, R., Young, C., Tsai, C., Pikelnaya, O., and Stutz, J.: Quantifying Nitrous Acid Formation Mechanisms Using Measured Vertical Profiles During the CalNex 2010 Campaign and 1D Column Modeling, Journal of Geophysical Research: Atmospheres, 126, e2021JD034689, https://doi.org/10.1029/2021JD034689, 2021.
VandenBoer, T. C., Young, C. J., Talukdar, R. K., Markovic, M. Z., Brown, S. S., Roberts, J. M., and Murphy, J. G.: Nocturnal loss and daytime source of nitrous acid through reactive uptake and displacement, Nat Geosci, 8, 55-60, 10.1038/ngeo2298, 2015.

VandenBoer, T. C., Brown, S. S., Murphy, J. G., Keene, W. C., Young, C. J., Pszenny, A. A. P., Kim, S., Warneke, C., de Gouw, J. A., Maben, J. R., Wagner, N. L., Riedel, T. P., Thornton, J. A., Wolfe, D. E., Dubé, W. P., Öztürk, F., Brock, C. A., Grossberg, N., Lefer, B., Lerner, B., Middlebrook, A. M., and Roberts, J. M.: Understanding the role of the ground surface in HONO vertical structure: High resolution vertical profiles during NACHTT-11, Journal of Geophysical Research: Atmospheres, 118, 10,155-110,171, https://doi.org/10.1002/jgrd.50721, 2013.

Vogel, B., Vogel, H., Kleffmann, J., and Kurtenbach, R.: Measured and simulated vertical profiles of nitrous acid - Part II. Model simulations and indications for a photolytic source, Atmos Environ, 37, 2957-2966, 10.1016/s1352-2310(03)00243-7, 2003.

Wang, H., Huang, C., Tao, W., Gao, Y., Wang, S., Jing, S., Wang, W., Yan, R., Wang, Q., An, J., Tian, J., Hu, Q., Lou, S., Pöschl, U., Cheng, Y., and Su, H.: Seasonality and reduced nitric oxide titration dominated ozone increase during COVID-19 lockdown in eastern China, npj Climate and Atmospheric Science, 5, 24, 10.1038/s41612-022-00249-3, 2022.

Wang, N., Lyu, X. P., Deng, X. J., Huang, X., Jiang, F., and Ding, A. J.: Aggravating O3 pollution due to NOx emission control in eastern China, Sci Total Environ, 677, 732-744, 10.1016/j.scitotenv.2019.04.388, 2019.

Wang, Y. A., Fu, X., Wu, D. M., Wang, M. D., Lu, K. D., Mu, Y. J., Liu, Z. G., Zhang, Y. H., and Wang, T.: Agricultural Fertilization Aggravates Air Pollution by Stimulating Soil Nitrous Acid Emissions at High Soil Moisture, Environ Sci Technol, 55, 14556-14566, 10.1021/acs.est.1c04134, 2021.

Weber, B., Wu, D. M., Tamm, A., Ruckteschler, N., Rodriguez-Caballero, E., Steinkamp, J., Meusel, H., Elbert, W., Behrendt, T., Sorgel, M., Cheng, Y. F., Crutzen, P. J., Su, H., and Poschi, U.: Biological soil crusts accelerate the nitrogen cycle through large NO and HONO emissions in drylands, P Natl Acad Sci USA, 112, 15384-15389, 10.1073/pnas.1515818112, 2015.

Wong, K. W., Tsai, C., Lefer, B., Grossberg, N., and Stutz, J.: Modeling of daytime HONO vertical gradients during SHARP 2009, Atmos Chem Phys, 13, 3587-3601, 10.5194/acp-13-3587-2013, 2013.

Xia, D. M., Zhang, X. R., Chen, J. W., Tong, S. R., Xie, H. B., Wang, Z. Y., Xu, T., Ge, M. F., and Allen, D. T.: Heterogeneous Formation of HONO Catalyzed by CO2, Environ Sci Technol, 55, 12215-12222, 10.1021/acs.est.1c02706, 2021.

Xing, C., Liu, C., Wang, S., Chan, K. L., Gao, Y., Huang, X., Su, W., Zhang, C., Dong, Y., Fan, G., Zhang, T., Chen, Z., Hu, Q., Su, H., Xie, Z., and Liu, J.: Observations of the vertical distributions of summertime atmospheric pollutants and the corresponding ozone production in Shanghai, China, Atmos. Chem. Phys., 17, 14275-14289, 10.5194/acp-17-14275-2017, 2017.

25

Xing, C. Z., Liu, C., Hu, Q. H., Fu, Q. Y., Wang, S. S., Lin, H., Zhu, Y. Z., Wang, S. T., Wang, W. W., Javed, Z. S., Ji, X. G., and Liu, J. G.: Vertical distributions of wintertime atmospheric nitrogenous compounds and the corresponding OH radicals production in Leshan, southwest China, J Environ Sci-China, 105, 44-55, 10.1016/j.jes.2020.11.019, 2021.

Xu, W., Kuang, Y., Zhao, C., Tao, J., Zhao, G., Bian, Y., Yang, W., Yu, Y., Shen, C., Liang, L., Zhang, G., Lin, W., and Xu, X.: NH3-promoted hydrolysis of NO2 induces explosive growth in HONO, Atmos. Chem. Phys., 19, 10557-10570, 10.5194/acp-19-10557-2019, 2019.

Xu, Z., Wang, T., Wu, J., Xue, L., Chan, J., Zha, Q., Zhou, S., Louie, P. K. K., and Luk, C. W. Y.: Nitrous acid (HONO) in a polluted subtropical atmosphere: Seasonal variability, direct vehicle emissions and heterogeneous production at ground surface, Atmos Environ, 106, 100-109, https://doi.org/10.1016/j.atmosenv.2015.01.061, 2015.

Xue, C., Ye, C., Kleffmann, J., Zhang, W., He, X., Liu, P., Zhang, C., Zhao, X., Liu, C., Ma, Z., Liu, J., Wang, J., Lu, K., Catoire, V., Mellouki, A., and Mu, Y.: Atmospheric measurements at Mt. Tai – Part II: HONO budget and radical (ROx+NO3) chemistry in the lower boundary layer, Atmos. Chem. Phys., 22, 1035-1057, 10.5194/acp-22-1035-2022, 2022.

Xue, C., Ye, C., Zhang, C., Catoire, V., Liu, P., Gu, R., Zhang, J., Ma, Z., Zhao, X., Zhang, W., Ren, Y., Krysztofiak, G., Tong, S., Xue, L., An, J., Ge, M., Mellouki, A., and Mu, Y.: Evidence for Strong HONO Emission from Fertilized Agricultural Fields and its Remarkable Impact on Regional O3 Pollution in the Summer North China Plain, ACS Earth and Space Chemistry, 10.1021/acsearthspacechem.0c00314, 2021.

Xue, C. Y., Zhang, C. L., Ye, C., Liu, P. F., Catoire, V., Krysztofiak, G., Chen, H., Ren, Y. G., Zhao, X. X., Wang, J. H., Zhang, F., Zhang, C. X., Zhang, J. W., An, J. L., Wang, T., Chen, J. M., Kleffmann, J., Mellouki, A., and Mu, Y. J.: HONO Budget and Its Role in Nitrate Formation in the Rural North China Plain, Environ Sci Technol, 54, 11048-11057, 2020.

Yang, W. J., You, D., Li, C. H., Han, C., Tang, N., Yang, H., and Xue, X. X.: Photolysis of Nitroaromatic Compounds under Sunlight: A Possible Daytime Photochemical Source of Nitrous Acid?, Environmental Science & Technology Letters, 8, 747-752, 10.1021/acs.estlett.1c00614, 2021a.

Yang, X. P., Lu, K. D., Ma, X. F., Liu, Y. H., Wang, H. C., Hu, R. Z., Li, X., Lou, S. R., Chen, S. Y., Dong, H. B., Wang, F. Y., Wang, Y. H., Zhang, G. X., Li, S. L., Yang, S. D., Yang, Y. M., Kuang, C. L., Tan, Z. F., Chen, X. R., Qiu, P. P., Zeng, L. M., Xie, P. H., and Zhang, Y. H.: Observations and modeling of OH and HO2 radicals in Chengdu, China in summer 2019, Sci Total Environ, 772, 12, 10.1016/j.scitotenv.2020.144829, 2021b.

Yang, Y. M., Li, X., Zu, K. X., Lian, C. F., Chen, S. Y., Dong, H. B., Feng, M., Liu, H. F., Liu, J. W., Lu, K. D., Lu, S. H., Ma, X. F., Song, D. L., Wang, W. G., Yang, S. D., Yang, X. P., Yu, X. N., Zhu, Y., Zeng, L. M., Tan, Q. W., and Zhang, Y. H.: Elucidating the effect of HONO on O-3 pollution by a case study in southwest China, Sci Total Environ, 756, 13, 10.1016/j.scitotenv.2020.144127, 2021c.

Ye, C., Zhou, X., Pu, D., Stutz, J., Festa, J., Spolaor, M., Tsai, C., Cantrell, C., Mauldin, R. L., Campos, T., Weinheimer, A., Hornbrook, R. S., Apel, E. C., Guenther, A., Kaser, L., Yuan, B., Karl, T., Haggerty, J., Hall, S., Ullmann, K., Smith, J. N., Ortega, J., and Knote, C.: Rapid cycling of reactive nitrogen in the marine boundary layer, Nature, 532, 489-491, 10.1038/nature17195, 2016.

Ye, C. X., Zhang, N., Gao, H. L., and Zhou, X. L.: Photolysis of Particulate Nitrate as a Source of HONO and NOx, Environ Sci Technol, 51, 6849-6856, 2017.

Zhang, G. X., Hu, R. Z., Xie, P. H., Lou, S. R., Wang, F. Y., Wang, Y. H., Qin, M., Li, X., Liu, X. Y., Wang, Y., and Liu, W. Q.: Observation and simulation of HOx radicals in an urban area in Shanghai, China, Sci Total Environ, 810, 11, 10.1016/j.scitotenv.2021.152275, 2022a.

26

Zhang, J., Lian, C., Wang, W., Ge, M., Guo, Y., Ran, H., Zhang, Y., Zheng, F., Fan, X., Yan, C., Daellenbach, K. R., Liu, Y., Kulmala, M., and An, J.: Amplified role of potential HONO sources in O3 formation in North China Plain during autumn haze aggravating processes, Atmos. Chem. Phys., 22, 3275-3302, 10.5194/acp-22-3275-2022, 2022b2022a.

Zhang, L., Wang, T., Zhang, Q., Zheng, J. Y., Xu, Z., and Lv, M. Y.: Potential sources of nitrous acid (HONO) and their impacts on ozone: A WRF-Chem study in a polluted subtropical region, J Geophys Res-Atmos, 121, 3645-3662, 10.1002/2015jd024468, 2016.

Zhang, W. Q., Tong, S. R., Lin, D., Li, F. J., Zhang, X. R., Wang, L. L., Ji, D. S., Tang, G. Q., Liu, Z. R., Hu, B., and Ge, M. F.: Atmospheric chemistry of nitrous acid and its effects on hydroxyl radical and ozone at the urban area of Beijing in early spring 2021, Environ Pollut, 316, 9, 10.1016/j.envpol.2022.120710, 2023.

Zhang, W. Q., Tong, S. R., Jia, C. H., Ge, M. F., Ji, D. S., Zhang, C. L., Liu, P. F., Zhao, X. X., Mu, Y. J., Hu, B., Wang, L. L., Tang, G. Q., Li, X., Li, W. R., and Wang, Z.: Effect of Different Combustion Processes on Atmospheric NitrousAcid Formation Mechanisms: A Winter Comparative Observation inUrban, Suburban and Rural Areas of the North China Plain, Environ Sci Technol, 56, 4828-4837, 10.1021/acs.est.1c07784, 2022c2022b.

Zhang, X. R., Tong, S. R., Jia, C. H., Zhang, W. Q., Li, J., Wang, W. G., Sun, Y. L., Wang, X., Wang, L. L., Ji, D. S., Wang, L. L., Zhao, P. S., Tang, G. Q., Xin, J. Y., Li, A., and Ge, M. F.: The Levels and Sources of Nitrous Acid (HONO) in Winter of Beijing and Sanmenxia, J Geophys Res-Atmos, 127, 16, 10.1029/2021jd036278, 2022d2022c.

Zhao, Y., Zhang, K., Xu, X., Shen, H., Zhu, X., Zhang, Y., Hu, Y., and Shen, G.: Substantial Changes in Nitrogen Dioxide and Ozone after Excluding Meteorological Impacts during the COVID-19 Outbreak in Mainland China, Environmental Science & Technology Letters, 7, 402-408, 10.1021/acs.estlett.0c00304, 2020.

Zhou, X., Gao, H., He, Y., Huang, G., Bertman, S. B., Civerolo, K., and Schwab, J.: Nitric acid photolysis on surfaces in low-NOx environments: Significant atmospheric implications, Geophys Res Lett, 30, https://doi.org/10.1029/2003GL018620, 2003.

Zhou, X., Zhang, N., TerAvest, M., Tang, D., Hou, J., Bertman, S., Alaghmand, M., Shepson, P. B., Carroll, M. A., Griffith, S., Dusanter, S., and Stevens, P. S.: Nitric acid photolysis on forest canopy surface as a source for tropospheric nitrous acid, Nat Geosci, 4, 440-443, 10.1038/ngeo1164, 2011.
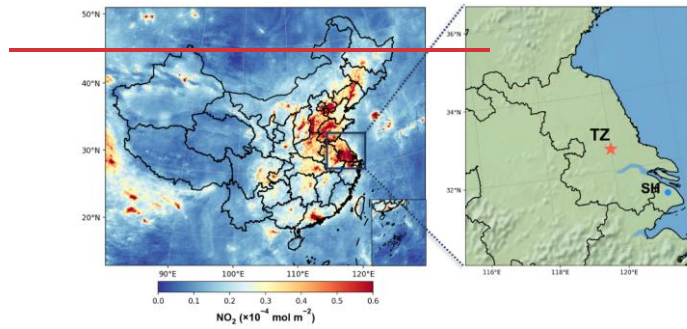
Figure 1: Location of the field measurement site (red star) in Taizhou (TZ), Jiangsu Province. This site is situated approximately 200 km northwest of Shanghai (SH), one megacity in YRD. The left map is colored by monthly average NO$_2$ column density retrieved from TROPOMI (July, 2018).
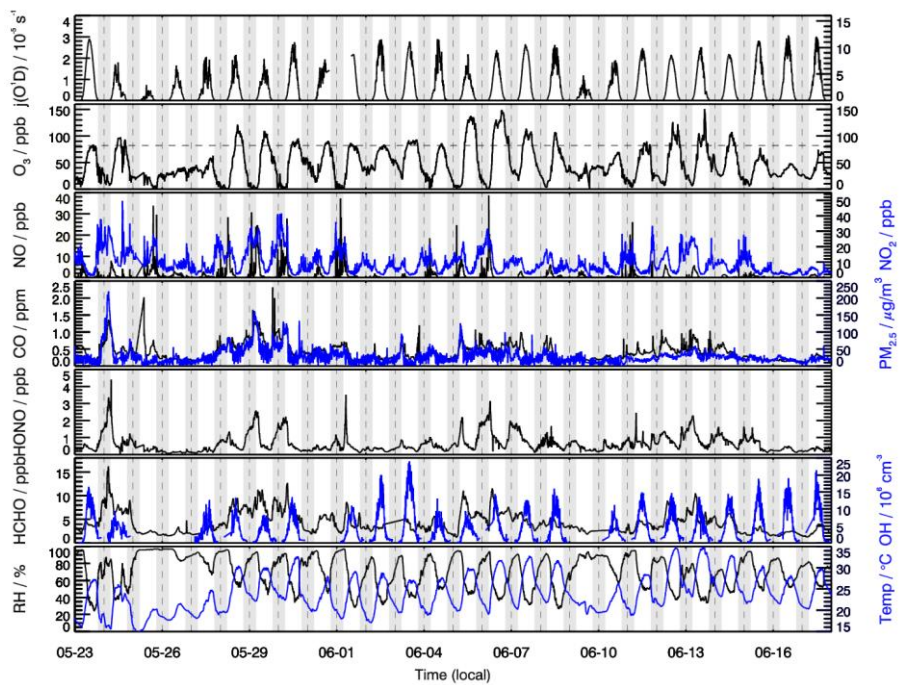
965

29
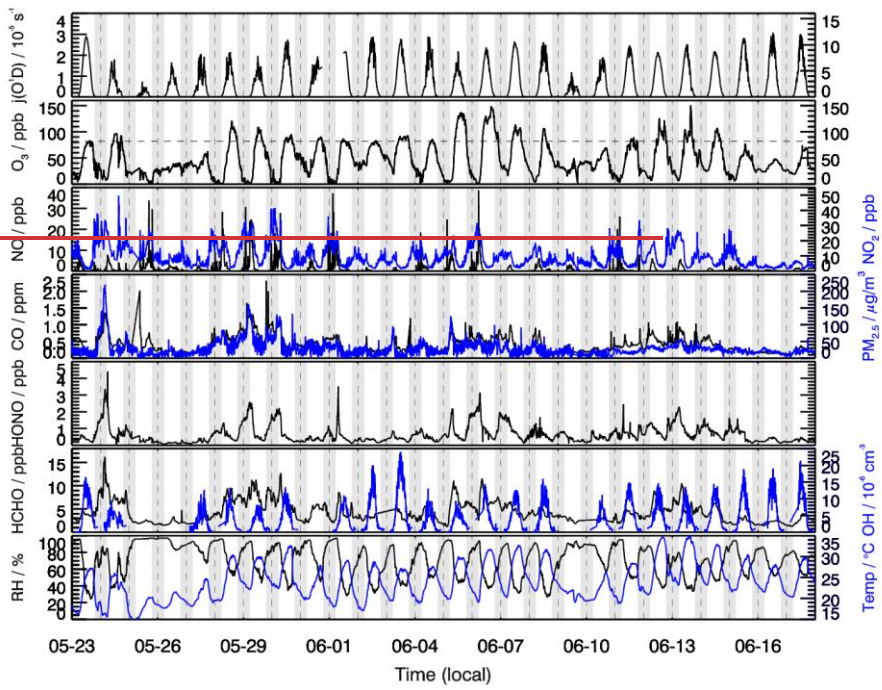
Figure 21: Time series of HONO, O₃, CO, PM₂.₅, OH, HCHO, NOₓ, relative humidity (RH), temperature and j(O¹D) during the EXPLORE-YRD campaign.
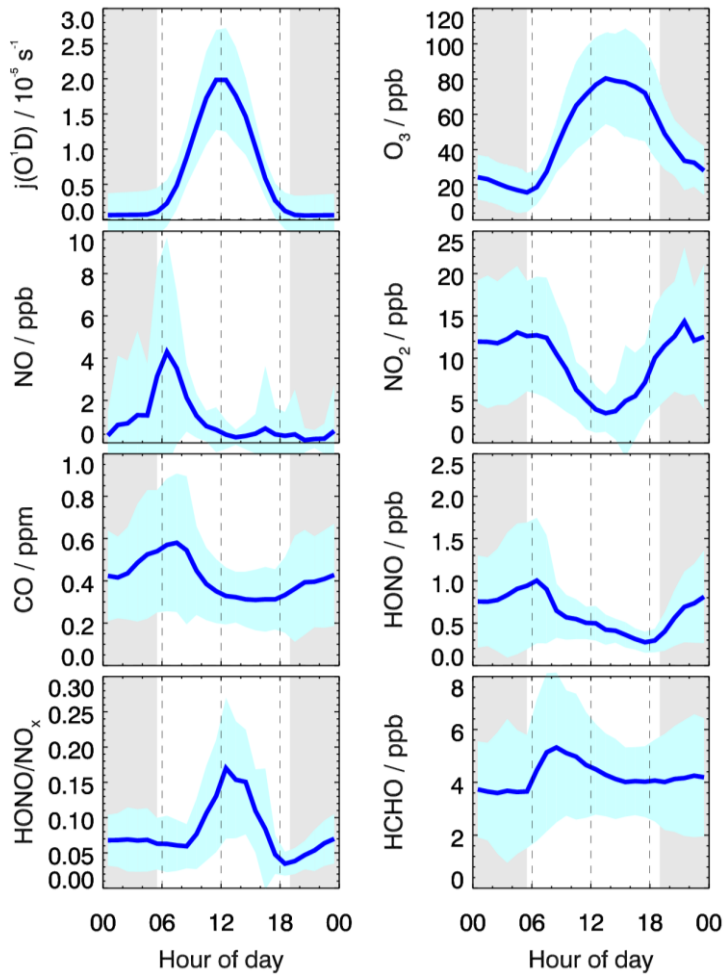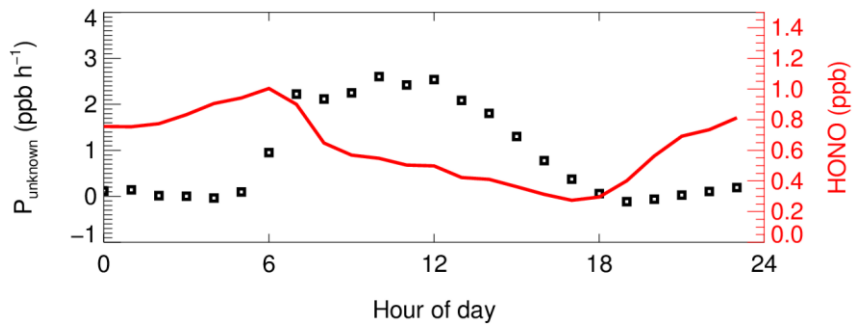
970

975

980

Figure 32: The diurnal patterns of HONO, HONO/NOx, NO, NO2, CO, O3, HCHO and j(O1D).

985

Figure 43: The diurnal profiles of calculated HONO unknown source ($P_{unknown}$) strength and observed HONO.

990

995

1000

1005

32
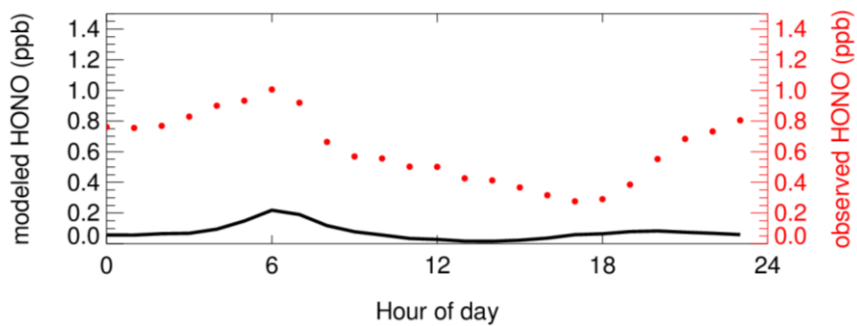
1010

Figure 54: The modeled HONO concentration with only default HONO source (OH+NO).

1015

1020

1025

1030

33
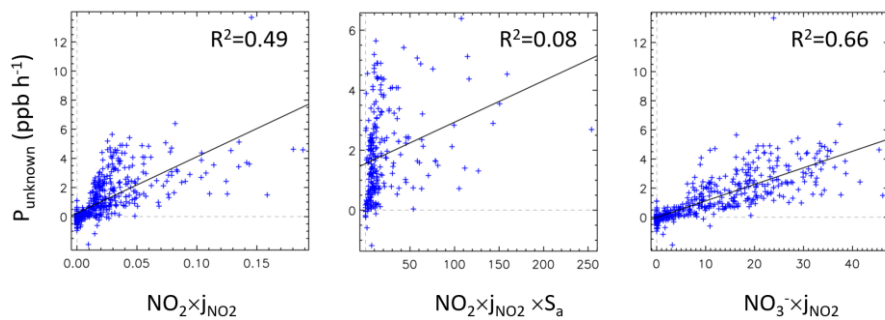
1035

Figure 65: The unknown source strength (P$_{unknown}$, 8:00-18:00) plotted against NO$_2$×j(NO$_2$), NO$_2$×j(NO$_2$)×S$_a$ and NO$_3^-$×j(NO$_2$).

1040

1045

34
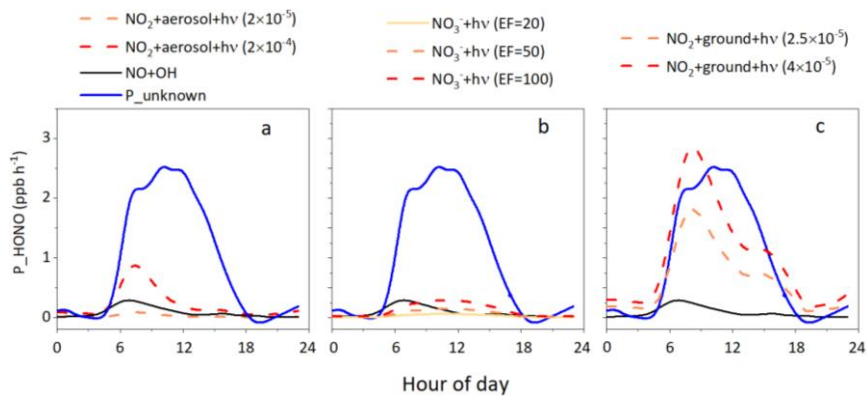
Figure 7̶6: HONO production rates by different HONO formation pathways with different parameter settings. (a) photo-induced NO₂ conversion on the aerosol surface; (b) heterogeneous particulate nitrate photolysis; (c) photo-induced NO₂ conversion on the ground surface.
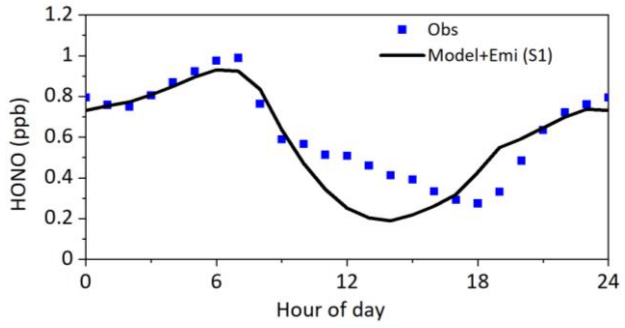
Figure 87: Modeled HONO concentrations with additional HONO sources compared to the observations. Model+Emi represents the sum of modeled HONO and vehicle HONO emission.
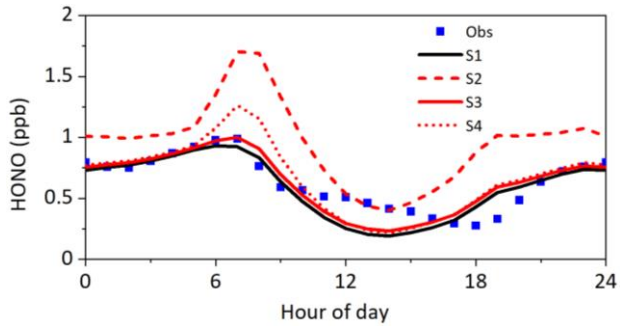
1075

1080

1085

1090

1095

Figure 98: Results from sensitivity tests compared with observed HONO concentrations. S1: parameters were listed in Table 1; S2: $\gamma_{ground+h\nu}$ was changed to 6×10^{-5} compared to S1; S3: $\gamma_{aerosol+h\nu}$ was changed to 2×10^{-4} compared to S1; S4: EF was changed to 120 compared to S1.
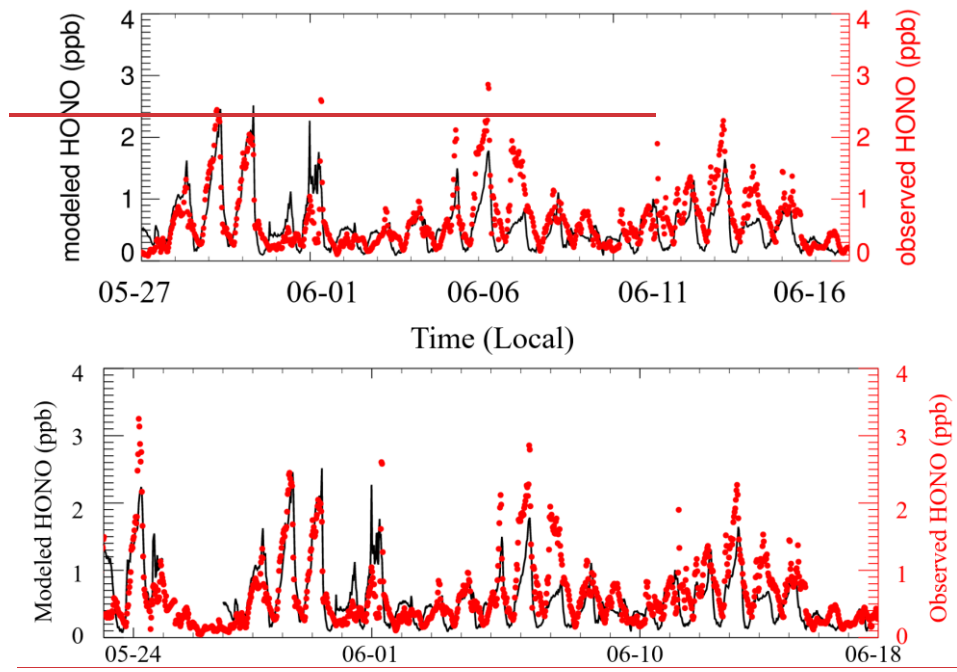
Figure ~~10~~9: Time series of modeled and observed HONO concentrations from 05-~~27~~ 23 to 06-~~16~~18.
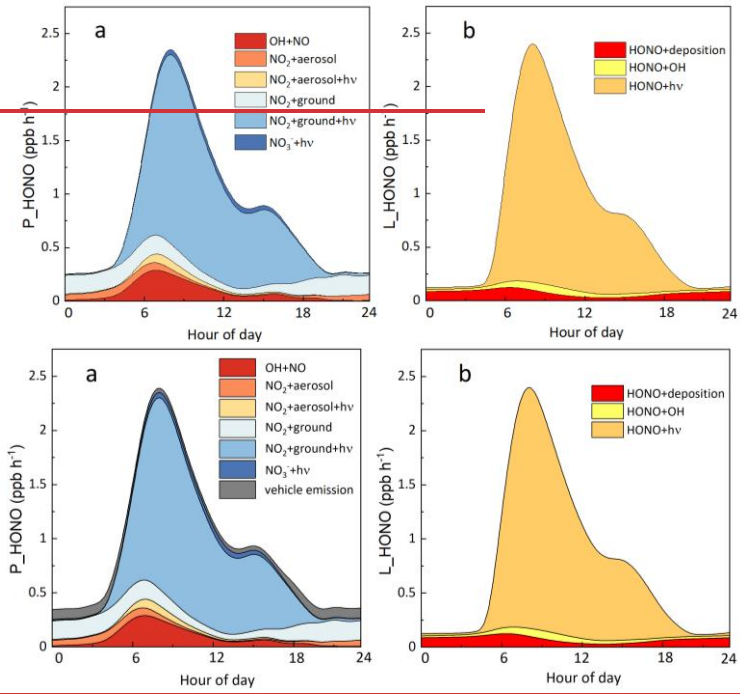
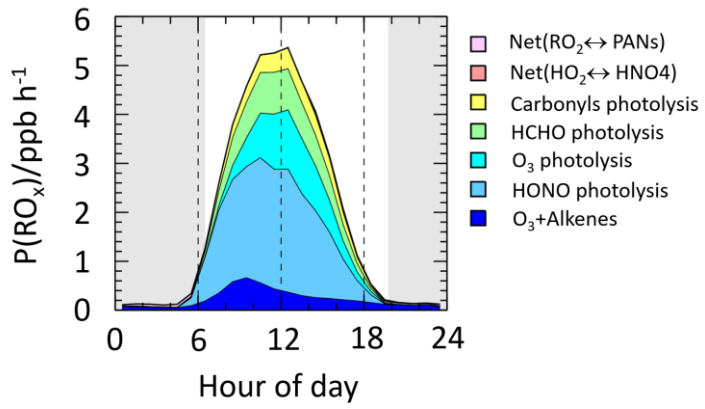1125

1130

1135

Figure ~~11~~10: HONO production rates and loss rates by different pathways.
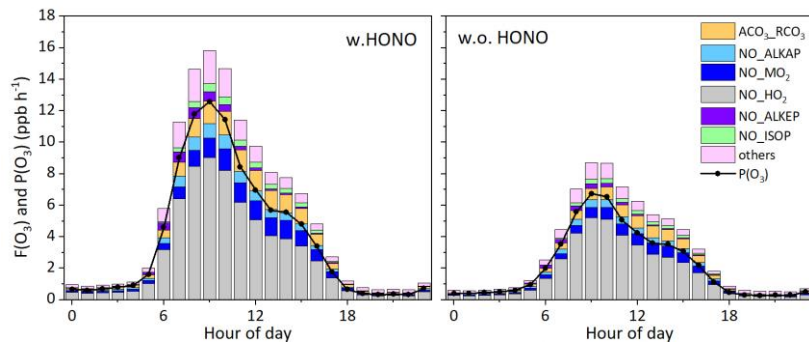
1140

Figure ~~12~~11: Primary RO$_x$ production rates by different pathways during the EXPLORE-YRD campaign.

1145

1150

1155

1160

1165

Figure ~~13~~12: Model-calculated total and net O$_3$ production rate with and without observed HONO as a model constraint. According to different type of VOC precursors, organic peroxy radicals (RO$_2$) can be classified into seven categories, including methyl peroxy radicals (MO$_2$=CH$_3$O$_2$), first-generation peroxy radicals from alkanes (ALKAP), alkenes except isoprene (ALKEP), isoprene (ISOP), aromatics (AROP), OVOC (OVOCP) and acyl peroxy radicals (ACETYLP=ACO$_3$+RCO$_3$).

1170

1175

1180

1185

Table 1. Parameterized HONO source mechanisms in the box model.

Mechanisms	Reaction	Parameterization
NO_2 hydrolysis on the aerosol surface	$NO_2+\text{aerosol}\rightarrow 0.5HONO$	$\gamma_{aerosol}=1\times 10^{-5}$
Photo-induced NO_2 conversion on the aerosol surface	$NO_2+\text{aerosol}\xrightarrow{h\nu} HONO$	$\gamma_{aerosol+h\nu}=2\times 10^{-5}$
NO_2 hydrolysis on the ground surface	$NO_2+\text{ground}\rightarrow 0.5HONO$	$\gamma_{ground}=2\times 10^{-6}$
Photo-induced NO_2 conversion on the ground surface	$NO_2+\text{ground}\xrightarrow{h\nu} HONO$	$\gamma_{ground+h\nu}=2.5\times 10^{-5}$
Nitrate photolysis	$NO_3^-\xrightarrow{h\nu} HONO$	$EF=20$

Table 2. Different model simulation scenarios and corresponding configuration.

Scenario	Configuration
S0	Default HONO formation mechanism (OH+NO)
S1	S0+five heterogeneous source (parameters set as Table 1) +emission
S2	$\gamma_{ground+h\nu}$ was changed to 6×10^{-5} compared to S1
S3	$\gamma_{aerosol+h\nu}$ was changed to 2×10^{-4} compared to S1
S4	EF was changed to 120 compared to S1